Hydrological drivers of bedload transport in an Alpine watershed

G. Antoniazza[1,2], T. Nicollier[2], S. Boss[2], F. Mettra[3], A. Badoux[2], B. Schaefli[4], D. Rickenmann[2] and S. N. Lane[1]

[1]Institute of Earth Surface Dynamics (IDYST), University of Lausanne, Lausanne, Switzerland.

[2]Mountain Hydrology and Mass Movements, Swiss Federal Research Institute WSL, Birmensdorf, Switzerland.

[3]Ecological Engineering Laboratory (ECOL), Environmental Engineering Institute (IIE), School of Architecture, Civil and Environmental Engineering (ENAC), Ecole Polytechnique Fédérale de Lausanne (EPFL), Lausanne, Switzerland.

[4]Institute of Geography (GIUB) and Oeschger Center for Climate Change Research (OCCR), University of Bern, Switzerland.

Corresponding author: Gilles Antoniazza (gilles.antoniazza@unil.ch)

Key-points

- The co-occurrence of rainfall in a watershed where the snowmelt signal is strong was the largely dominant driver of bedload transport.
- Melt-only events and rainfall events occurring once the melt signal has become smaller were drivers of secondary importance.
- Combined rain and snowmelt, and melt-only drivers of bedload transport, may decrease due to climate change impacts on Alpine hydrology.

This article has been accepted for publication and undergone full peer review but has not been through the copyediting, typesetting, pagination and proofreading process, which may lead to differences between this version and the Version of Record. Please cite this article as doi: 10.1029/2021WR030663.

Abstract

Understanding and predicting bedload transport is an important element of watershed management. Yet, predictions of bedload remain uncertain by up to several order(s) of magnitude. In this contribution, we use a five-year continuous time-series of streamflow and bedload transport monitoring in a 13.4 km^2 snow-dominated Alpine watershed in the Western Swiss Alps to investigate hydrological drivers of bedload transport. Following a calibration of the bedload sensors, and a quantification of the hydraulic forcing of streamflow upon bedload, a hydrological analysis is performed to identify daily flow hydrographs influenced by different hydrological drivers: rainfall, snowmelt, and combined rain and snowmelt events. We then quantify their respective contribution to bedload transport. Results emphasize the importance of combined rain and snowmelt events, for both annual bedload volumes (77% on average) and peaks in bedload transport rate. A non-negligible, but smaller, amount of bedload transport may occur during late summer and autumn storms, once the snowmelt contribution and baseflow have significantly decreased (9% of the annual volume on average). Although rainfall-driven changes in flow hydrographs are responsible for a large majority of the annual bedload volumes (86% on average), the identified melt-only events also represent a substantial contribution (14 % on average). The results of this study help to improve current predictions of bedload transport through a better understanding of the bedload magnitude-frequency relationship under different hydrological conditions. We further discuss how bedload transport could evolve under a changing climate through its effects on Alpine watershed hydrology.

Plain language summary

Understanding and predicting bedload transport is an important element of watershed management. Yet, it remains a challenge to predict bedload transport accurately. In this paper, we profit from a rare five-year continuous time-series of streamflow and bedload transport in a 13.4 km^2 snow-dominated Alpine watershed in the Western Swiss Alps to investigate the hydrological drivers of bedload transport. An analysis of the streamflow time-series together with meteorological data allows classification of daily flow hydrographs over the five years of observation between rainfall-driven, melt-driven, and a combination of both, and quantification of their contribution with regards to bedload transport. Results of the study show that combined rainfall and snowmelt events with high baseflow are the dominant driver of bedload transport (77% of annual bedload on average), followed to a lower extent by rainfall occurring in the late summer and autumn (9% of annual bedload on average), when the melt contribution and baseflow are lower. The results of this study help to improve current predictions of bedload transport through a better understanding of the bedload magnitude-frequency relationship under different hydrological conditions. We further discuss how bedload transport could evolve under a changing climate through its effects on Alpine watershed hydrology.

Key-words

Bedload transport; Alpine watershed; Hydrological drivers; Rainfall; Snowmelt; Climate change.

1. Introduction

Bedload transport in Alpine watersheds is a serious natural hazard, which can be costly in economic terms and potential loss of life (e.g. Badoux et al., 2016, 2014a). It often requires river engineering and represents a challenge for land-use planning (e.g. Heritage et al., 2019; Sims and Rutherfurd, 2017) and hydropower production (e.g. OFEV, 2021; Pralong et al., 2015; Speerli et al., 2020). It also has a direct impact on the ecology of river systems (Badoux et al., 2014b; FOEN, 2021; Gabbud et al., 2019; Hauer et al., 2018; Lane et al., 2020; Wang et al., 2014). These aspects are of particular concern for the current management of river systems, but also for their future with regards to the evolution of bedload dynamics under a rapidly changing climate.

Despite decades of development of bedload transport models, best estimates of bedload transport rates still suffer from at least one order of magnitude of error (Ancey, 2020a, 2020b; Recking, 2013; Schneider et al., 2015; Yager et al., 2015). The challenge of bedload transport prediction derives partly from the fact that it is a complex process to express physically (Ancey, 2020a; Ashworth and Ferguson, 1986; Buffington and Montgomery, 1997; Gomez, 1991; Gomez and Church, 1989; Parker et al., 1982), bedload being the balance between changing sediment transport capacity (as a function of changing streamflow; e.g. Rickenmann, 2020, 2018), but also changing sediment availability (both at the streambed and as supply from the drainage network; e.g. Comiti et al., 2019; Kammerlander et al., 2017; Piton and Recking, 2017). In addition, it is also extremely challenging to measure in natural settings, and so to obtain the data needed to determine the level of complexity in bedload transport models. Direct sampling devices (e.g. Bunte et al., 2004; Helley and Smith, 1971) may be hazardous to deploy and only provide at-a-point data in time and space. They also commonly require the signal (or at least its variance) to be known in order to determine a reliable sampling frequency (Bunte and Abt, 2005; Gomez, 1991; Gomez et al., 1989; Parker et al., 1982; Singh et al., 2009). Measurements of the rate of filling of traps or reservoirs dug across streams provided cross-sectional integrated estimates of sediment loads, including during high flows (Gray et al., 2010; Hinderer et al., 2013; Lane et al., 2017; Lenzi et al., 1999). Yet, their resolution depends on the rate at which trap-filling is measured, leading to time-series of low temporal resolution (e.g. load per event in the best case, but more common are annual loads; e.g. Hinderer et al., 2013).

Indirect passive sensors have allowed new perspectives for bedload transport monitoring (Rickenmann, 2017). The noise produced by bedload particles in motion can be captured by underwater microphones (e.g. Barton et al., 2010; Geay et al., 2017; Rigby et al., 2016), by out-of-bank seismometers (e.g. Burtin et al., 2008; Dietze et al., 2019; Roth et al., 2016) or by measuring the vibration of a structure (e.g. plate, pipe) impacted by bedload particles in motion (e.g Dell'Agnese et al., 2014; Downing, 2010; Mao et al., 2016; Mizuyama et al., 2010; Perolo et al., 2019; Rickenmann et al., 2014). Such approaches may provide continuous time-series of bedload transport at high temporal resolution (i.e. down to 1 second), covering both high and low flow conditions (Rickenmann, 2017); and also absolute fluxes if the sensors can be calibrated (e.g. Dell'Agnese et al., 2014; Mao et al., 2016; Nicollier et al., 2021; Rickenmann et al., 2012).

Continuous, high-resolution records allow quantification of relationships between bedload transport and discharge (Rickenmann, 2018) as well as evaluation and development of bedload transport models (e.g. Rickenmann, 2020). Such studies have confirmed in field settings the

inherent autogenic variability of bedload transport observed in laboratory flumes (Gomez et al., 1989; Hoey and Sutherland, 1991) over short time-periods (i.e. less than a couple of hours; Rickenmann, 2018). Over longer time-periods, stronger correlations between streamflow and bedload transport rate emerge (Rickenmann, 2020, 2018). They suggest at such time-scales some forcing of bedload transport by exogenic controls such as watershed hydrology, and associated hydraulic transport capacity. In the meantime, the relationship remains dependent on sediment supply conditions, both from the streambed and from the surrounding drainage network (Buffington and Montgomery, 1997; Mao, 2018, 2012; Mao et al., 2014; Masteller et al., 2019; Rickenmann, 2020).

Within Alpine watersheds, a range of hydrological processes can lead to streamflow variations, and so trigger bedload transport if the transport capacity is sufficient, and sediment is available. These hydrological processes notably include ice and snowmelt, rainfall, and the co- occurrence of rainfall and snowmelt events, which include "rain-on-snow" (ROS) events (Corripio and López-Moreno, 2017; Li et al., 2019; Musselman et al., 2018). Despite the increasing number of bedload transport time-series measured within Alpine watersheds, there are very few studies (e.g. Dell'Agnese et al., 2015; Mao, 2012; Rainato et al., 2017) that have related temporal variations in bedload transport to possible hydrological drivers, and their respective contribution to annual bedload budgets. This matters not only for improving our ability to predict bedload transport under current climatic conditions, but also for predicting how bedload transport may evolve with climate change impacts on the hydrology of Alpine watersheds.

The goal of this paper is to relate bedload volumes exported from an Alpine watershed to hydrological drivers (e.g. snowmelt, rainfall, combined rainfall and snowmelt events). The analysis is based on a five-year (2016-2020) bedload time-series recorded with passive acoustic sensing using a Swiss Plate Geophone system (e.g. Rickenmann, 2017). The system is installed in the stream that drains the Vallon de Nant, a snowmelt-dominated Alpine watershed in the Western Swiss Alps. After calibration, the time-series of bedload transport were associated with streamflow and classified into the different hydrological categories (i.e. snowmelt, rainfall, co-occurrence of rain and snowmelt) likely dominant at different time-periods throughout the year. This allows us to tease out the contribution of different hydrological drivers to bedload transport and, using knowledge of likely future changes in watershed hydrology under a warming climate, assess possible evolution in bedload transport.

2. Material and methods

2.1 The Vallon de Nant watershed

The Vallon de Nant (VdN) is a 13.4 km^2 watershed located in the western Swiss Alps (Figure 1), with elevations ranging from c. 1200 to 3050 m a.s.l. Although ~ 3 % of the watershed surface is occupied by the debris-covered Glacier des Martinets, it provides only small amounts of ice melt and the hydrological regime of the Avançon de Nant (AdN), the Alpine stream that drains the VdN, is dominated by snowmelt (Ceperley et al., 2020; Mächler et al., 2021; Michelon et al., 2021; Thornton et al., 2021). The AdN flows from the glacier snout (2313 m a.s.l) over a length of ~ 6.5 km to a hydrological and bedload monitoring station (1200 m a.s.l) installed at the watershed outlet. The average gradient of the AdN is c. 17 %, but varies (8-29 %) over its course, including braided reaches with lower slopes and steeper step-pool and semi-alluvial reaches (Figure 1). It is fed by ~10 intermittent, steep (40-60%), torrential tributaries that mainly flow during the snowmelt season or briefly during storm events, and which form

large coalescent fans at the hillslope base (Figure1; Lane et al., 2016). Most of the exported sediment is expected to come from the large capacity-limited braided areas along the AdN main course, notably found in the upper half of the watershed, and which are well connected down to the outlet. These are fed by torrential tributaries. In addition, between the braided zones and the measurement station there are additional torrential tributaries, which may only be well connected during low-frequency high-magnitude events. The steeper step-pool and semi-alluvial channels in the lower half of the watershed are expected to convey sediment and may be dominated by supply-limited conditions (Figure 1).

During the period 2014-2015, a hydrological and bedload monitoring station was built at the outlet of the watershed (1200 m a.s.l), through a collaboration between the University of Lausanne (FGSE), the Swiss Federal Institute for Forest, Snow and Landscape Research WSL and the ETH Zürich (Physics of Environmental Systems). Details of the monitoring station are given in the sections below.

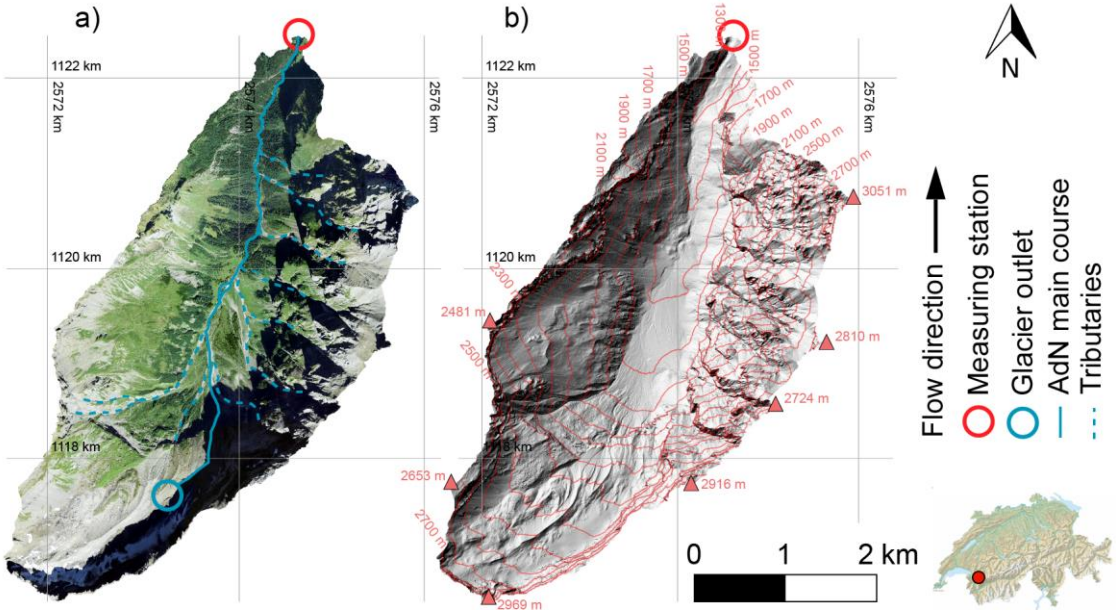

Figure 1. The 13.4-km^2 VdN watershed with the Glacier des Martinets outlet (blue circle), and the monitoring station at the outlet (red circle). In a) aerial image from 2013. In b) hillshade of the Swiss Alti3d digital elevation model (Acknowledgments © Swisstopo). Coordinates are in the CH1903 Swiss system.

2.2 Streamflow monitoring

Streamflow data were derived from a radar-based stage sensor (Vegapuls WL 61). The sensor was mounted on a steel arm extended (Figure 2b), over a trapezoidal concrete cross-section installed in the stream and where neither erosion nor deposition could occur. The transit time of the radar pulses from emission to reception allows estimation of the distance to the water surface. Knowing the height of the sensor above the streambed (1.83 m), absolute water depths can be derived. The sensor records at a sampling rate of ~ 0.5 s, and data were averaged over 1 minute. Globally, the water depth measurement has been reliable throughout the period of interest (2016-2020), with the exception of discrete periods of time where the measurement failed and the data are missing. Missing streamflow data are notably found in the winter period,

during which the AdN channel is sometimes covered by ice and snow, biasing the water height sensing. Thus, an equivalent of 80 full days are missing over the 1827 days of the period of observation, and 72 % of the missing data occur in the winter period (December to March), where bedload activity is typically very low (i.e. 98.8 % of the total bedload occurred outside the missing discharge data window).

A calibration is required to transform the measured water depths [m] into a streamflow per unit time [$l \cdot s^{-1}$]. Salt gauging was performed at the VdN monitoring station to build a rating curve between measured water depths and streamflow (Ceperley et al., 2018). During the years 2016 and 2017, 56 salt gauging samples were collected for water depths varying between 0.05 and 0.3 m. The relationship between water depth and streamflow was best expressed by a power law rating curve (Ceperley et al., 2018):

$$Q = 19998 * d^{1.6244} \qquad [1]$$

where Q is the streamflow per unit time [$l \cdot s^{-1}$] and d is the water depth [m], with an R^2 of 0.91. This equation is in close agreement with a theoretical discharge, resulting from the Poleni formula applied to trapezoidal cross-sections (Bollrich, 2000; Ceperley et al., 2018).

2.3 Bedload monitoring

A Swiss Plate Geophone (SPG) system developed by the Swiss Federal Research Institute WSL was used in this research (e.g. Nicollier et al., 2021; Rickenmann et al., 2014; Wyss et al., 2016a). The SPG system is typically made of a line of steel plates embedded across a river channel. Bedload particles in motion induce a vibration of the steel plates, which is recorded by a geophone sensor mounted below each plate (Rickenmann, 2017). The response of the SPG system under various conditions (e.g. impact magnitude, transport intensities, flow velocities, grain-size mixture) has been investigated in both laboratory and field experiments (Antoniazza et al., 2020; Nicollier et al., 2021; Wyss et al., 2016a, 2016b, 2016c), and successful calibrations of the SPG system using independent concurrent sampling of bedload have been achieved for multiple monitoring stations (Habersack et al., 2017; Kreisler et al., 2017; Nicollier et al., 2021, 2020, 2019; Rickenmann et al., 2012; Rickenmann and Fritschi, 2017).

At the VdN monitoring station, 10 plates of the SPG system were mounted side-by-side across the channel width (Figure 2b, 2c). The plates are made of stainless steel and have a standardized size of 492 mm in width, 358 mm in length (in flow direction), and 15 mm in thickness, with a total mass of 21 kg (Antoniazza et al., 2020; Rickenmann, 2017; Rickenmann et al., 2012; Wyss et al., 2016a). The plates are mounted in a steel frame, which is embodied in a concrete check dam across the channel (Figure 2b, 2c). The plates are mounted flush with the riverbed upstream to avoid biasing approach flow conditions. Below each plate, a 20 DX geophone sensor from Geospace technologies (Houston, Texas, USA) is mounted in a PC801 LPC Landcase set in an aluminum box (Rickenmann et al., 2017, 2012), and the plates are isolated from each other with elastomer elements.

During bedload transport events, particles rolling, sliding and saltating over the SPG system produce impact shocks that generate a change in the electrical voltage sensed by the geophone. The geophone signal was found to be proportional to the total mass of bedload in transport (Rickenmann et al., 2014, 2012; Rickenmann and Fritschi, 2017). The SPG is connected to an industrial PC that records the geophone signal at a frequency of 10 kHz. Geophone data are then summarized in the number of impulses per minute, which corresponds to the number of times the geophone raw electrical signal exceeds a pre-defined threshold. In previous studies of

bedload transport using the SPG system (e.g. Antoniazza et al., 2020; Rickenmann et al., 2014, 2012; Rickenmann and Fritschi, 2017), this threshold was set to 0.1 V in order to include the smallest detectable grain-size fractions (~10-20 mm), whilst at the same time being greater by at least one order of magnitude than the noise level for flow conditions without bedload transport. Over the period 2016-2020, an equivalent of 30 full days are considered as unreliable SPG monitoring. Of these, ~ 10 are days whose data have to be excluded due to work on the measurement station, although these were almost always days with no bedload transport activity. The remaining missing data correspond to ~20 days of power failure at the monitoring station.

2.4 Geophone calibration

The Swiss Plate Geophone (SPG) system requires a robust calibration to transform the recorded signal into an actual mass of bedload in transport. This is typically achieved by collecting bedload samples during natural transport events that can be directly related to the signal measured by the sensors (Nicollier et al., 2021, 2020, 2019; Rickenmann et al., 2014, 2012; Rickenmann and Fritschi, 2017).

At the VdN, we used a mobile sediment basket to collect the calibration samples (Figure 2a). The sediment basket was mounted with rollers on a rail fixed on the downstream side of the concrete weir where the SPG are imbedded. Using a system of ropes and pulleys, the sediment basket was moved along the rail and located directly downstream of a given plate. Doing so, every particle that impacts this plate can be collected in the sediment basket. For this purpose, the sediment basket (530 mm) was slightly wider than a SPG (492 mm). The sediment basket had an initial capacity of ~ 100 kg, but we expanded it during the calibration sampling by removing the downstream-facing panel and replacing it by a net that increased the sampling capacity to ~ 500 kg (Figure 2a). A removable lid was also built for the basket to prevent the collection of particles while positioning the basket at the plate targeted for calibration (Figure 2c).

Every bedload sample was collected using the following protocol: (a) the sediment basket (with the net extension) was emptied of sediment, covered with the lid and placed at the true right end of the rail (Figure 2a); (b) one operator standing on the true left bank pulled the basket until it was positioned directly downstream of the targeted SPG. Marks on the ropes on both basket sides allowed precise basket positioning (± 0.01 m). Once positioned, ropes were secured on both banks to keep the basket stable during bedload sampling; (c) on the true right bank, a second operator removed the basket lid whilst a third operator simultaneously started the geophone raw recording (10 kHz) from the station laptop; (d) particles that impacted the targeted plate fell into the basket and progressively filled up the extension net. Bedload sampling lasted between 40 seconds and 10 minutes according to the intensity of bedload transport; (e) once the sampling time had elapsed and/or the sampling net was sufficiently filled, the second and third operators rapidly pulled the basket back using the ropes. Pulling back the basket typically lasted 2 to 3 seconds, which minimized the risk of collecting additional unwanted particles while bringing the basket back to the bank position; (f) all the bedload particles collected in the basket and extension net were emptied to labelled storage boxes (i.e. sample number, name of the associated calibration file, number of the calibrated plate, sampling duration).

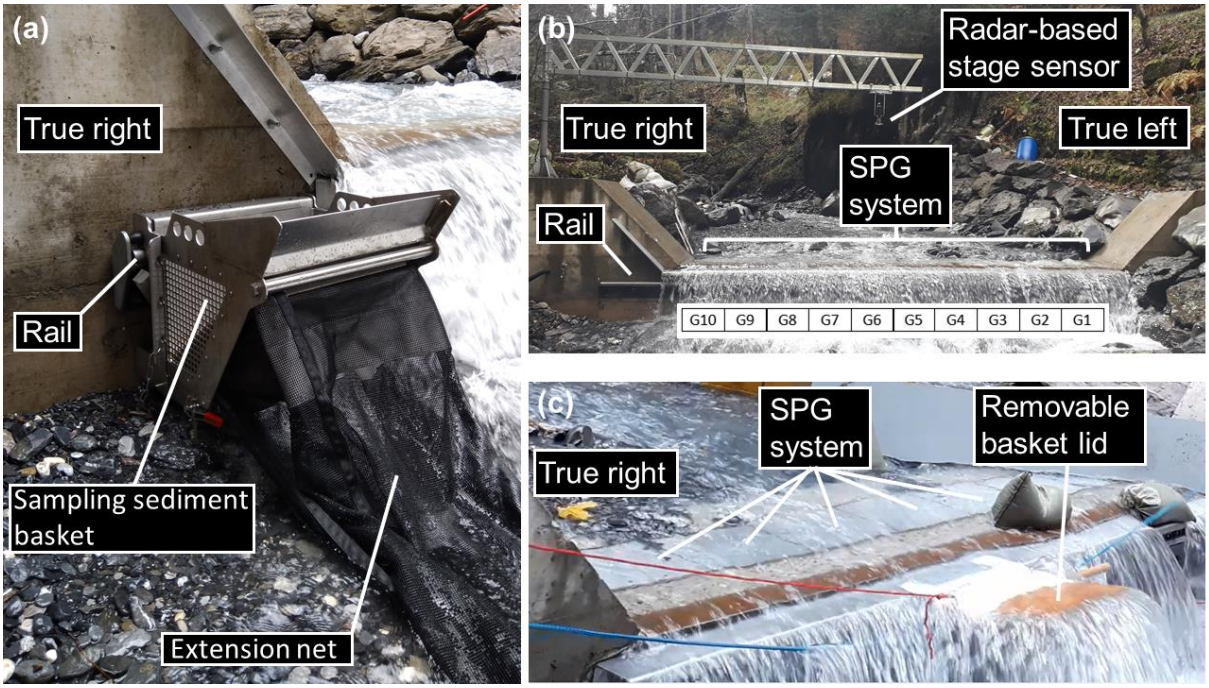

Figure 2. (a) The sediment sampling basket (with the extension net) placed on the rail; (b) General view of the VdN monitoring station. The radar-based stage sensor monitoring the water surface is set above the stream at the end of a steel arm. Geophone plates are labelled G1 to G10 from the true left to true right bank. The rail that supports the mobile sediment basket is visible to the left of the waterfall; (c) View of the SPG system along the concrete weir, and of the sediment sampling basket in experiment conditions. The blue ropes are used to pull the basket across the section. The red rope is used to remove the lid at the start of a sampling.

Calibration samples were collected during four days of fieldwork distributed within the 2019 and 2020 snowmelt seasons (details for each calibration sample are available in Supporting Information S1). The specific fieldwork days were picked in order to have a range of flow (and so bedload transport) conditions with sampled discharges ranging from 0.88 to 2.69 $m^3 \cdot s^{-1}$. In total, 55 bedload samples were collected using the mobile sediment basket. Samples were alternatively collected over plates G5, G6, G7 and G8. This choice was motivated by a range of reasons. First, an impact experiment conducted over every SPG showed that all the plates at the VdN monitoring station responded similarly to impacts of comparable magnitude (Antoniazza et al., 2020); hence, a unique calibration coefficient could be used for all the different plates at this site (i.e. equations [2] and [3] below). Second, plates G5, G6, G7 and G8 recorded together ~ 69 % of the total bedload transport during the investigated period (2016-2020).

In previous studies to calibrate the SPG system in the field, the sampled bedload mass M_{tot} (Rickenmann et al., 2014, 2012; Rickenmann and McArdell, 2008, 2007; Wyss et al., 2016c) or the unit bedload transport rate q_b (Habersack et al., 2017; Kreisler et al., 2017; Rickenmann, 2018; Rickenmann et al., 2020; Rickenmann and Fritschi, 2017) were related to the number of impulses N_{imp} or to the impulse rate *IMPT*, respectively, and typically for particles with a diameter larger than 19 mm. This limit was retained for its closeness to the threshold of detection of the SPG system (~10-20 mm). In our samples, particles between 9.5 and 19 mm represent on average ~13% of the total mass.

After collection, bedload samples were brought from the field to the laboratory of the Swiss Federal Research Institute WSL, and were sieved to include only particles greater than 19 mm. Each sample was then weighted using an industrial scale (precision of 10^{-3} kg). The mass of each sample is reported in Supplementary Information S1, together with the number of impulses N_{imp} exceeding 0.1 V (Antoniazza et al., 2020; Rickenmann et al., 2014, 2012). The average grain-size distribution of the calibration samples is also provided in Supplementary Information S1 (Figure S1.1).

Previous research on the calibration of the SPG system (e.g. Nicollier et al., 2021, 2020, 2019; Rickenmann et al., 2014, 2012; Rickenmann and Fritschi, 2017) found that the mass of the material that impacted a given plate could be linearly related to the number of impulses recorded by the associated geophone sensor, i.e. :

$$M_{\text{tot}} = c_1 * N_{\text{imp}} \qquad [2]$$

where M_{tot} [kg] is the mass of material that impacted a given plate, c_1 [kg] is a field-site dependent constant and N_{imp} $[-]$ is the recorded number of impulses.

Knowing the sampling duration (Supplementary Information S1) and the width over which bedload occurs (i.e. roughly 0.5 m of plate width), the relationship can also be expressed in terms of rates, such as:

$$q_{\text{b}} = c_2 * IMPT \qquad [3]$$

Where q_{b} is a unit transport rate [kg·min^{-1}·m^{-1}], c_2 [kg·m^{-1}] is a field-site dependent constant, and *IMPT* an impulse rate [min^{-1}].

In this paper, a linear regression line was fitted through the origin and the 55 calibration samples for both absolute and rate values. Linear relationships have indeed shown to perform well for most of the sites equipped with the SPG system, notably in Switzerland and Austria (e.g. Rickenmann, 2018; Rickenmann et al., 2014, 2012; Rickenmann and Fritschi, 2017). The slope of the relationship gives the c_1 and c_2 coefficients, and a R^2 was calculated. The 95% confidence intervals were also calculated as:

$$CI = \pm t \sqrt{\frac{\sum e^2}{n-2}\left[\frac{1}{n} + \frac{(x_0-\bar{x})^2}{\sum x^2 - n\bar{x}^2}\right]} \qquad [4]$$

where t is the t-value of Student, e are the residual values, n is the number of calibration samples, x_0 are the values of the independent variable N_{imp} in the time-series, x are the values of the independent variable N_{imp} in the calibration set, and $\bar{x}$ is the mean of x. When bedload masses are summed over a given time-period (e.g. months, years), the associated uncertainty is calculated following a summation rule:

$$\sigma_{\text{mass}} = \pm t \left[\sum_{i=1}^{T} {CI_i}^2\right]^{0.5} \qquad [5]$$

where σ_{mass} [kg] is the uncertainty in mass summed over a time-period T. In this paper, bedload masses were estimated with a 95 % confidence interval, with $t = 1.96$.

In Figure 3a and 3b, the relationships between the number of impulses N_{imp} and the bedload mass M_{tot} on the one hand, and between the impulse rate *IMPT* and the unit transport rate q_{b} on the other hand, are best expressed by a linear regression passing through the origin. The slope

coefficients were 0.066 for total mass (c_1) and 0.073 for unit transport rate (c_2) and the R^2 were 0.85 and 0.88 respectively. The collection of calibration samples over a wide range of impulses (i.e. 99.4 % of 1-minute data points with bedload over the five-year time-series fall within the calibration domain) further allows narrow confidence intervals over most of the domain of interest, which translates into transport rate uncertainties that are low compared to the transport rates themselves.

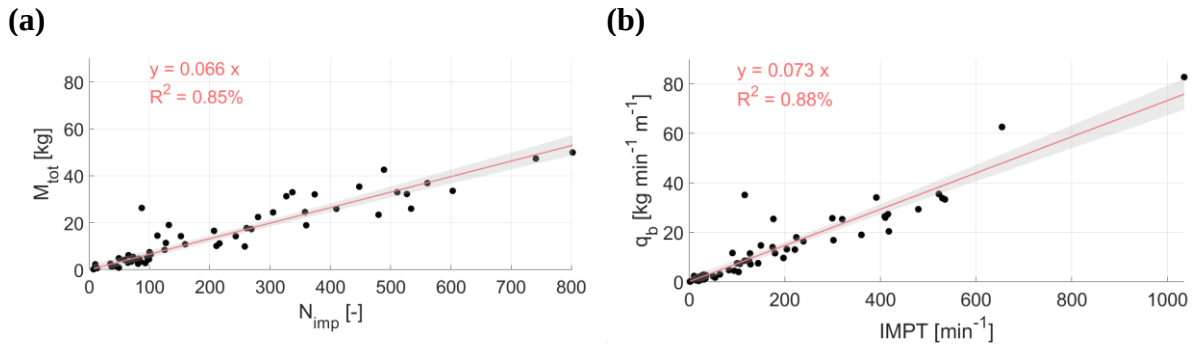

Figure 3. Calibration relationship derived from 55 bedload samples (> 19 mm) at the VdN in (a) absolute (with coefficient c_1) and (b) rate terms (with coefficient c_2). The shaded area gives the 95% confidence intervals calculated from [4], which are used to propagate the uncertainty into transformed bedload mass and unit bedload transport rates. The fit was forced through 0 using the 'polyfitzero' Matlab function (Mikovski, 2021).

Earlier studies interested in the calibration of the SPG system found that slope coefficients c_1 and c_2 may vary according to a range of factors, which include flow velocity (Nicollier et al., 2021; Wyss et al., 2016a, 2016b), bed roughness (Wyss et al., 2016a, 2016b) and particle grain size (Nicollier et al., 2021; Wyss et al., 2016c). Furthermore, an impact experiment conducted by Antoniazza et al. (2020) at several bedload monitoring sites equipped with the SPG system (including the VdN) showed that ~10-20% of the signal recorded on a given impacted plate propagates into the neighbouring non-impacted plates despite the isolating elastomer elements. These elements likely influence the relationship between the SPG impulse count and the actual mass of bedload in transport shown in the scatter in Figure 3. Nevertheless, these sources of variability are implicitly included in the slope coefficients proposed here, the bedload samples being collected for a range of natural streamflow and bedload transport rates that covers various flow conditions, grain-size distribution and rates of signal propagation. The scatter is moreover relatively low. Therefore, the calibration of the SPG system presented here is considered to be reliable.

2.5 Data analysis

The quantification of bedload transport over the five years of observation (2016-2020), and the identification of the hydrological events driving them it, were performed through three main complementary analyses.

2.5.1 Bedload and hydraulic forcing

First, absolute time-series of bedload transport over the period of interest, together with the streamflow time-series, were computed. Bedload transport was then integrated across different time-scales (e.g. years, months) to quantify its variability. Annual erosion rates were also derived from the total volume of bedload exported for comparison with other watersheds where such data are available.

In addition, an estimate of the hydraulic forcing of bedload transport at the VdN was performed, by comparing daily measured bedload transport with the daily predicted one, based on transport capacity calculations. The transport capacity calculations used a set of shear stress-based sediment transport equations proposed in the work of Schneider et al. (2015) and Rickenmann (2020), which have been shown to perform relatively well in Alpine streams with comparable characteristics to the Avançon de Nant. A total shear stress approach combined with a slope-dependent reference shear stress was used as it was shown to perform as well as other treatments, such as a constant reference shear stress combined with a reduced shear stress (e.g. Rickenmann, 2020; Schneider et al., 2015). A reference shear stress approach was preferred to an excess (unit) discharge or excess shear stress approach because the latter was shown to produce a much too steep increase in the transport capacity with increasing unit discharge or increasing dimensionless shear stress (e.g. Rickenmann, 2018). The set of equations represents a modified form of the Wilcock and Crowe (2003) equation, which predicts daily bedload transport rate Q_b [kg·s^{-1}] (of particles greater than 4 mm) using the total shear stress (i.e. transport capacity-based), and integrating bedload transport over the entire channel width:

$$W^* = 0.002\left(\frac{\tau^*_{D50}}{\tau^*_{rD50}}\right)^{16.1} \quad \text{for } \frac{\tau^*_{D50}}{\tau^*_{rD50}} < 1.143 \text{ and D} > 4 \text{ mm} \qquad [6.1]$$

$$W^* = 14\left(1 - \frac{0.85}{\left(\frac{\tau^*_{D50}}{\tau^*_{rD50}}\right)^{0.7}}\right)^{4.5} \quad \text{for } \frac{\tau^*_{D50}}{\tau^*_{rD50}} \geq 1.143 \text{ and D} > 4 \text{ mm} \qquad [6.2]$$

where $W^*$is the dimensionless transport rate, and where the dimensionless bed shear stress τ^*_{D50}, the dimensionless reference bed shear stress τ^*_{rD50} and the total transport rate Q_b [kg·s^{-1}] are defined as:

$$\tau^*_{D50} = \frac{r_h S}{R D_{50}} \qquad [7]$$

$$\tau^*_{rD50} = 0.56\, S^{0.5} \qquad [8]$$

$$Q_\mathrm{b} = b * \rho_s * W^* * \frac{(g * r_h * S)^{1.5}}{R * g} \qquad [9]$$

In the set of equations, r_h [m] is the hydraulic radius, S [-] is the channel gradient, $R = \rho_s/\rho - 1$ [-] is the relative sediment density (with the sediment density $\rho_s = 2650$ kg/m^3 and the water density $\rho = 1000$ kg/m^3), D_{50} [m] is the median of the surface grain-size distribution, $g = 9.81$ [m/s^2] is the gravitational acceleration.

In this study, the ~20 m long natural reach upstream of the monitoring station was selected to perform the calculations, because the hydraulic conditions within that reach were considered more representative than those at the weir to calculate the bedload transport capacity. In this reach, a mean slope S of 0.04 was measured in a total station survey, the median of the bed grain-size distribution $D_{50} = 0.06$ m was estimated through line-by-number counts on emerged areas of the bed (e.g. bars) using a 7 pixels per cm resolution orthophoto. The hydraulic radius $r_h = (b + mh)h\,/\,(b + 2h * \sqrt{1 + m^2})$ was estimated for every 1-min measured water depth h [m] within the trapezoidal natural channel cross-section. In the calculations, $b = 5.8\,m$ is the average channel width, and $m = h$ / *tan(45)* = h is the increase in channel width [m] with depth

[m], with the slope of the channel banks set to 1:1. Additional details on the reach over which the transport capacity calculations are performed, as well as details on the calculation of the representative classes of the streambed grain-size distribution, are provided in Supplementary Information S2.

In order to calculate the hydraulic conditions in the natural section upstream of the monitoring station, discharge measurements were combined with the flow resistance equations proposed in Rickenmann and Recking (2011), with dimensionless mean flow velocity U^{**} and discharge q^{**}:

$$U^{**} = 1.443 * \ {q^{**}}^{0.6} \left[1 + \left(\frac{q^{**}}{43.78}\right)^{0.8214}\right]^{-02435} \quad [10.1]$$

$$U^{**} = \frac{U}{\sqrt{g*S*D_{84}}} \quad [10.2]$$

$$q^{**} = \frac{Q/b}{\sqrt{g*S*{D_{84}}^3}} \quad [10.3]$$

$$h = \ D_{84} * m_1 * {q^{**}}^{m_2} \quad [10.4]$$

where U is the depth-averaged flow velocity [m/s], Q is the discharge measured at the monitoring station [m^3/s] and D_{84} = 0.36 m is the 84th percentile of grain-size distribution, estimated following the same procedure than the D_{50}. Coefficients $m_1 = 1.6^{-1}$ and $m_2 = 0.455$ follow Rickenmann and Recking (2011). Once Q_b was calculated for every 1-minute time-step, it was then integrated over each day to obtain daily predicted bedload masses.

2.5.2 Classification of the hydrological drivers of bedload

The contribution of different hydrological drivers to total bedload transport were identified in the streamflow time-series. We were particularly interested to investigate the proportion of bedload transported during rainfall-induced streamflow variations, during melt-induced streamflow variations, and during the co-occurrence of rainfall-induced and melt-induced streamflow variations, because these are the hydrological drivers expected to be able to trigger bedload transport, either separately or in combination.

The first step identified daily flow hydrographs influenced by rainfall. To do so, precipitation and temperature data were obtained from the RhiresD and TabsD datasets of MeteoSwiss. The RhiresD and TabsD datasets represent respectively daily precipitation (rainfall and snowfall equivalent, [mm]) and daily mean temperature [°C] interpolated at a spatial resolution of 1 km^2 from the dense precipitation-gauge and temperature sensor networks of MeteoSwiss (MeteoSwiss, 2019, 2017). Eighteen 1-km^2 cells of the RhiresD and TabsD grids covering partially or entirely the VdN were retained, and their coordinates are reported in Supplementary Information S3. From the RhireD precipitation dataset, a gross partitioning between rainfall and snowfall was performed, by summing for each grid cell the precipitation that occurred when the temperature of a given grid cell was above or below 1°C, respectively.

In an early stage of the work, an automatic classification of "rain-forced" and "not rain-forced" daily flow hydrographs was attempted, following Mutzner et al. (2015). It used a set of criteria combining the removal of snowy days (precipitation occurring during days where mean temperatures are below 1°C), the depth of rainfall (of days where mean temperatures are above

1°C), the amplitude of daily flow hydrographs and the timing throughout the day of high flows and low flows (i.e. to differentiate between rainfall-driven and melt-driven changes in daily flow hydrographs). However, no sensible set of criteria covering the range of flow hydrograph responses was identified using this approach, notably due to (1) the variable depth of rainfall generating a flow hydrograph response; (2) the variable daily mean temperature generating snowfall or rainfall (i.e. visible in the direct response to precipitation in the flow hydrograph); (3) the variable recession time of rainfall-driven events; and (4) a large variability in the amplitude and timing of daily low and high flows.

Therefore, a visual classification of the 1827 daily flow hydrographs into the two classes "rain-forced" and "not rain-forced" was undertaken. It used daily precipitation data, daily mean temperature data and daily flow hydrograph (i.e. amplitude, timing of high flows and low flows) to support the classification, but without setting fixed arbitrary thresholds in temperature, precipitation and/or the daily flow hydrograph, which were found to be unsuitable at the previous stage. Each daily flow hydrograph was first considered in terms of its amplitude and the timing of high flows and low flows. Then, daily precipitation and mean temperature data were used to determine whether any daily flow hydrograph was possibly influenced by rainfall. The daily flow hydrograph of the antecedent day was also systematically used to identify possible recession curves in the daily flow hydrograph of the subsequent day. This approach allowed inclusion within the "rain-forced" category of days where rainfall visually induced a response in the flow hydrograph, including potential recession curves in the subsequent day(s). Within the class "not rain-forced" daily flow hydrographs, it also allowed the inclusion of days with precipitation, but where the latter did not induce a response in the flow hydrograph. This may include snowfall, light rainfall or rainfall stored in a pre-existing snowpack or in the soil. Note that we are interested here in determining whether any daily flow hydrograph variation is (directly or indirectly) caused by rainfall, and not in the exact paths (e.g. surface water, subsurface water) the flow is following. Examples of typical daily flow hydrographs classified in each category (i.e. "rain-forced" or "not rain-forced") are provided in Supplementary Information S4. Annual flow hydrographs, variations in daily precipitations and daily mean temperatures for each year of observation (2016-2020) are available in Supplementary Information S5.

Once daily flow hydrographs influenced by rainfall were identified within the streamflow time-series of each year (2016-2020), we partitioned periods of the year with differing melt intensity. The method used to classify daily flow hydrographs according to melt intensity follows Mutzner et al. (2015), and is based on the amplitude of daily melt discharge cycles. To identify days with clear melt signal, only the previously classified "not rain-forced" days are considered (Figure S4.1b, S4.2b, S4.3b, S4.4b, S4.5b). For each "not rain-forced" day, a daily flow hydrograph variation was calculated by subtracting a 24-hour moving average from the measured streamflow, to obtain a so-called detrended flow hydrograph Q_{det} [$m^3 \cdot s^{-1}$] (Mutzner et al., 2015). The amplitude of the daily flow hydrograph cycle Q_{amp} [$m^3 \cdot s^{-1}$] was estimated as half the difference between the maximum and the minimum value in the detrended daily flow hydrograph (Gribovszki et al., 2010; Mutzner et al., 2015). A visual inspection of the variation in both Q_{det} (Figure S5.1c S5.2c, S5.3c, S5.4c, S5.5c) and Q_{amp} (Figure S5.1d, S5.2d, S5.3d, S5.4d, S5.5d) throughout each year permitted the identification of coherent periods of time when daily flow hydrographs of "not rain-forced" days would recurrently vary within a

comparable range (Figure 4). We labelled them the pre-melt period, the early-melt period, the high-melt period, the late-melt period, and the post-melt period.

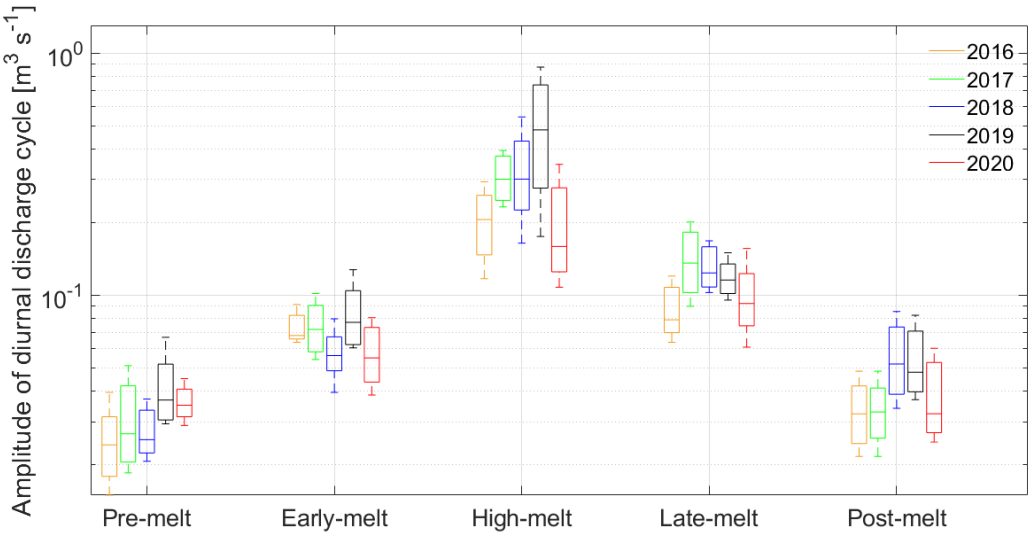

Figure 4. Distribution of daily Q_{amp} values (10th, 25th, 50th, 75th and 90th percentiles) within each period (i.e. pre-melt, early-melt, high-melt, late-melt, post-melt) for "not rain-forced" daily flow hydrographs of all investigated years (2016-2020).

At the VdN, the pre-melt period extends from January 1st to the onset of the melt season in early spring (i.e. April), and typically presents Q_{amp} median values between 0.02 and 0.04 [$m^3 \cdot s^{-1}$] (Figure 4; Table 1). The early-melt period represents the onset of the snowmelt season, during which the amplitude of the diurnal hydrograph cycles Q_{amp} remains however relatively low, with median values ranging between 0.06 and 0.08 [$m^3 \cdot s^{-1}$] (Figure 4; Table 1). The high-melt period is the period with high rates of snowmelt, during which the amplitude of the diurnal hydrographs is the highest, with median values typically greater than 0.16 [$m^3 \cdot s^{-1}$] (Figure 4; Table 1). The late-melt represents the period where a distinctive decrease in the amplitude of the diurnal hydrograph cycles is observed as the watershed snow content decreases, but where the remaining snowmelt still generates intermediate values of Q_{amp}, with median ranging from 0.08 to 0.14 [$m^3 \cdot s^{-1}$] (Figure 4; Table 1). The post-melt is the period where remaining melt from the previous winter no longer produces large variations in Q_{amp}, and where the amplitude of 'not rain-forced days' diurnal discharge hydrographs mainly relies on the evapotranspiration cycle, and/or the melt of the potential first winter snowfall. The post-melt period spans from the late summer until the end of the year, with median values typically ranging between 0.03 and 0.05 [$m^3 \cdot s^{-1}$]. The determined date of the start and end of each period for each year, and the distribution of Q_{amp} values within them are reported in Table 1. Results of the classification (Table 1; Figure 4) show on the one hand the relatively low overlap between Q_{amp} values of different periods within the same year. On the other hand, it exhibits a remarkable consistency of Q_{amp} values within a same period across years. It is important to note that given the specific meteorological conditions (e.g. temperatures, snow volumes) of a given year, the different periods may start and end at very different dates (Table 1). If the pre-melt and post-melt periods do present a distribution of daily discharge amplitude that varies within a comparable range, they are quite different in terms of watershed hydrology and bedload dynamics. Indeed, the pre-

melt corresponds to a rather cold period with a great amount of snow in the watershed, while the post-melt includes autumn storms, a more prominent evapotranspiration cycle, and the potential occurrence of the first winter snowfall in a watershed mostly free of snow cover. This is why we keep the two periods separated.

Table 1. Dates of start and end of the five identified periods (pre-melt, early-melt, high-melt, late-melt, post-melt) for each investigated year, determined based on the range of variability in Q_{amp} values (25$^{\mathrm{th}}$, 50$^{\mathrm{th}}$ and 75$^{\mathrm{th}}$ percentile value reported here), and a visual inspection of the variation of both Q_{det} (Figure S5.1c S5.2c, S5.3c, S5.4c, S5.5c) and Q_{amp} through time (Figure S5.1d, S5.2d, S5.3d, S5.4d, S5.d).

		Pre-melt 50$^{\mathrm{th}}$ [25$^{\mathrm{th}}$, 75$^{\mathrm{th}}$]	**Early-melt 50$^{\mathrm{th}}$ [25$^{\mathrm{th}}$, 75$^{\mathrm{th}}$]**	**High-melt 50$^{\mathrm{th}}$ [25$^{\mathrm{th}}$, 75$^{\mathrm{th}}$]**	**Late-melt 50$^{\mathrm{th}}$ [25$^{\mathrm{th}}$, 75$^{\mathrm{th}}$]**	**Post-melt 50$^{\mathrm{th}}$ [25$^{\mathrm{th}}$, 75$^{\mathrm{th}}$]**
2016	Dates	**Jan. 1$^{\mathrm{st}}$ – Apr.10$^{\mathrm{th}}$**	**Apr. 11$^{\mathrm{th}}$ – May 5$^{\mathrm{th}}$**	**May 6$^{\mathrm{th}}$ – Aug. 11$^{\mathrm{th}}$**	**Aug. 12$^{\mathrm{th}}$ – Aug. 28$^{\mathrm{th}}$**	**Aug. 29$^{\mathrm{th}}$ – Dec. 31$^{\mathrm{th}}$**
	Q_{amp} [m^3 s^{-1}]	**0.02** [0.02, 0.03]	**0.07** [0.07, 0.08]	**0.21** [0.16, 0.25]	**0.08** [0.07, 0.1]	**0.03** [0.03, 0.04]
2017	Dates	**Jan. 1$^{\mathrm{st}}$ – Apr. 2$^{\mathrm{nd}}$**	**Apr. 3$^{\mathrm{rd}}$ – May 13$^{\mathrm{h}}$**	**May 14$^{\mathrm{th}}$ – Jun. 21$^{\mathrm{th}}$**	**Jun. 20$^{\mathrm{th}}$ – Sep. 4$^{\mathrm{th}}$**	**Sep. 5$^{\mathrm{th}}$ – Dec. 31$^{\mathrm{th}}$**
	Q_{amp} [m^3 s^{-1}]	**0.03** [0.02, 0.04]	**0.07** [0.06, 0.09]	**0.3** [0.25, 0.37]	**0.14** [0.1, 0.18]	**0.03** [0.03, 0.04]
2018	Dates	**Jan. 1$^{\mathrm{st}}$ – Apr. 7$^{\mathrm{th}}$**	**Apr. 8$^{\mathrm{th}}$ – Apr. 16$^{\mathrm{th}}$**	**Apr. 17$^{\mathrm{th}}$ – Jun. 24$^{\mathrm{th}}$**	**Jun. 25$^{\mathrm{th}}$ – Sep. 4$^{\mathrm{th}}$**	**Sep. 5$^{\mathrm{th}}$ – Dec. 31$^{\mathrm{th}}$**
	Q_{amp} [m^3 s^{-1}]	**0.03** [0.02, 0.03]	**0.06** [0.05, 0.06]	**0.3** [0.24, 0.4]	**0.12** [0.1, 0.16]	**0.05** [0.04, 0.07]
2019	Dates	**Jan. 1$^{\mathrm{st}}$ – Apr. 4$^{\mathrm{th}}$**	**Apr. 5$^{\mathrm{th}}$ – May. 15$^{\mathrm{th}}$**	**May. 16$^{\mathrm{th}}$ – Jul. 8$^{\mathrm{th}}$**	**Jul. 9$^{\mathrm{th}}$ – Aug. 29$^{\mathrm{th}}$**	**Aug. 30$^{\mathrm{th}}$ – Dec. 31$^{\mathrm{th}}$**
	Q_{amp} [m^3 s^{-1}]	**0.04** [0.03, 0.05]	**0.08** [0.06, 0.1]	**0.48** [0.31, 0.69]	**0.12** [0.1, 0.13]	**0.05** [0.04, 0.07]
2020	Dates	**Jan. 1$^{\mathrm{st}}$ – Apr. 4$^{\mathrm{rd}}$**	**Apr. 5$^{\mathrm{th}}$ – Apr. 9$^{\mathrm{th}}$**	**Apr. 10$^{\mathrm{th}}$ – Jul. 20$^{\mathrm{th}}$**	**Jul. 21$^{\mathrm{th}}$ – Sep. 5$^{\mathrm{th}}$**	**Sep. 6$^{\mathrm{th}}$ – Dec. 31$^{\mathrm{th}}$**
	Q_{amp} [m^3 s^{-1}]	**0.04** [0.03, 0.04]	**0.06** [0.05 0.07]	**0.16** [0.13, 0.25]	**0.09** [0.08, 0.11]	**0.03** [0.03, 0.05]

From this hydrological analysis, we were able to partition each year into the five periods of differing melt intensity (i.e. pre-melt, early-melt, high-melt, late-melt and post-melt), and also to establish within them whether rainfall was additionally influencing or not the daily flow hydrograph ("rain-forced" and "not rain-forced" days). Bedload could then be integrated along those different categories, separately or in combination, to investigate the proportion of bedload transport driven by the different hydrological categories (i.e. rainfall-induced, melt-induced or a combination of both). The classification further allowed determination of the magnitude-frequency of daily bedload transport at the VdN for the different hydrological categories. The magnitude of bedload transport is calculated for both the daily total bedload mass transported [kg], and for the daily maximum bedload rate reached [kg·min^{-1}]. The frequency is calculated from the number of days within a given category that equals or exceeds a given bedload magnitude.

2.5.3 Determination of erosion rates inferred from bedload transport

Third, it is common to divide sediment export volumes by the average sediment density (i.e. 2650 kg· m^{3-1}; Hinderer et al., 2013), and by the associated watershed area (i.e. 13.4 km^2), to give annual erosion rates inferred from bedload transport. Although such calculations assume that sediment was eroded in the year that it was exported, we perform them here for comparative purposes with other watersheds where such data are available. Note that in addition to bedload particles < 19 mm, the erosion rates presented here do not include the suspended load, which is likely to represent a substantial proportion of the annual total mechanical erosion. At the VdN, we estimate it to represent at least 50% of the sediment budget (e.g. Hinderer et al., 2013; Turowski et al., 2010).

3. Results

3.1 Absolute bedload time-series, transported masses and hydraulic forcing

Five years of measurement of streamflow and bedload transport rates are presented in Figure 5a. Streamflow follows the general trends expected for a snowmelt-dominated Alpine watershed at this altitude (Figure 4, Table 1), with low baseflow during the winter season (pre-melt), increasing slowly during April at the onset of the melt season (early-melt), and more steadily during late May-early June. Streamflow then peaks in the period June-July at the maximum of the snowmelt season (high-melt), and decreases progressively as watershed snow content declines through the summer season (late-melt), and autumn (post-melt). This general seasonal trend is disrupted by sudden storms, especially during the summer and the autumn, that can generate periods of short-duration high streamflow. As expected, bedload transport also occurs during periods of high-magnitude streamflow, either during the snowmelt season or during storms throughout the year, with the exception of the winter period, when the lowest bedload transport rates tend to be observed.

Annual bedload mass varies significantly among the five years of observation (Figure 5b). 2019 had a much higher annual bedload mass, with $3.75 \cdot 10^6$ kg ($\pm$ $3.29 \cdot 10^3$ kg), followed by the year 2018 with $1.62 \cdot 10^6$ kg ($\pm$ $1.95 \cdot 10^3$ kg). The years 2016, 2017 and 2020 recorded a lower total bedload mass with $0.30 \cdot 10^6$ kg ($\pm$ $1.51 \cdot 10^3$ kg), $0.52 \cdot 10^6$ kg ($\pm$ 1.57 10^3 kg) and $0.65 \cdot 10^6$ kg ($\pm$ $1.65 \cdot 10^3$ kg), respectively. Over the five years investigated, the average annual mass of bedload exported from the VdN is $1.37 \cdot 10^6$ kg ($\pm$ 1.99 10^3 kg). From 2016 to 2020, the average annual erosion rate inferred from bedload transport at the Vallon de Nant is 0.039 mm·y^{-1} ($\pm$ $5.6 \cdot 10^{-5}$ mm). Annual and monthly transported bedload masses throughout the five years of measurement, and their estimation uncertainty, are reported in Supporting Information S6.

The differences observed in the annual bedload yield at the VdN do not scale directly with either the total amount of precipitation (rainfall and/or snowfall) a given year received, or with mean annual temperatures (Figure 5b, 5c). The annual sum of RhiresD daily precipitation (over the 18 1-km^2 cells selected for the VdN; Table S3.1) shows indeed that the year 2020 received the greatest amount of precipitation (~1905 mm), followed by the years 2019 (~1825 mm), 2016 (~1810 mm), 2018 (~1610 mm) and 2017 (~1500 mm). A gross estimate of rainfall (i.e. sum of daily precipitation of RhiresD where daily mean temperature TabsD is equal or above 1°C) suggests that the year 2019 received the greatest amount of rainfall (~1125 mm), followed by the year 2020 (~1120 mm), 2016 (~1020 mm), 2017 (~850 mm) and 2018 (~625 mm). A

gross estimate of snowfall (i.e. sum of daily precipitation of RhiresD where daily mean temperature TabsD is equal or below 1°C) suggests that the year 2018 received the greatest amount of snow (~985 mm), followed by the year 2016 (~790 mm), 2020 (~785 mm), 2019 (~700 mm) and 2017 (~650 mm). Regarding the annual mean temperature, the three warmest years are indeed the three most active in terms of bedload transport (2019, 2018, 2020), but with proportions that do not really scale with temperature. This decorrelation between precipitation, temperature and bedload transport is notably expected to be due to temporary storage in different hydrological compartments of the watershed (e.g. soil, snowpack). Note that precipitation in the RhiresD dataset is expected to be underestimated due to snow undercatch (Freudiger et al., 2016).

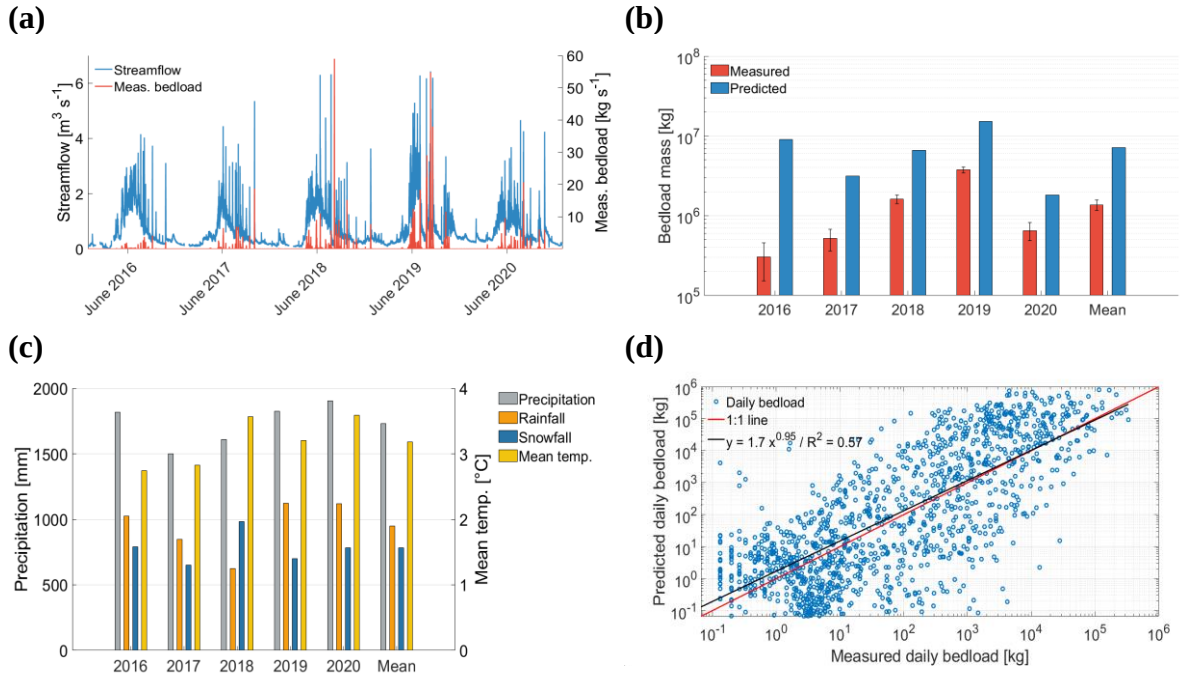

Figure 5. (a) Measured time-series of streamflow (in blue) and bedload transport rates (in red) over the five years of observation (2016-2020); (b) measured annual bedload masses (in red) predicted annual bedload masses (in blue) for each of the five years of observation. Note the logarithmic y-scale; (c) annual mean temperature (in yellow), precipitation (in gray), rainfall (in orange), snowfall (in dark blue), for each of the five years of observation; (d) relationship between daily predicted and daily measured bedload transport over the five years of observation. The red line is the 1:1 relationship, and the black line is the best-fit power law regression.

Regarding the shear stress-based estimate of bedload, calculated from equations [6-10] (Figure 5b, in blue), the hydraulic forcing based on time-integrated transport capacity tends to overestimate the actual measured bedload (Figure 5b, in red), with factors between 3 (2020) and 30 (2016) of difference. Part of the overestimation is due to the difference between the threshold of detection of the SPG system (particles of 10-20 mm) and the grain-size domain under which the equations [6-10] were validated (particles > 4 mm). Whilst these differences are substantial, our estimations remain somehow lower than many bedload predictions, which typically exceed bedload measurements by one or more order(s) of magnitude (Ancey, 2020a, 2020b; Recking, 2013; Schneider et al., 2015; Yager et al., 2015). Comparing the relative difference between years, the annual predicted bedload mass seems to scale approximatively

for the years 2017-2020, but not for the year 2016, with regards to relative yearly differences in the measured bedload mass (Figure 5b).

The relationship between the daily bedload mass derived from the SPG system measurements, and the daily bedload mass predicted from the time-integrated shear stress (i.e. transport capacity) equations is presented in Figure 5d. The relationship shows a relatively good agreement with the 1:1 line, with the exponent of the power law regression being close to 1, and an R^2 of 0.57, which illustrates the importance of hydraulic forcing for bedload transport. Yet, transport capacity calculations may be sensitive to the measurement of parameters *b*, *S*, D_{50} and D_{84} in equations [6-10], which also contain uncertainties. Thus, a Monte Carlo sensitivity analysis was performed by combining random values of these parameters (within a plausible range) to evaluate how they affect the transport capacity calculations. Details on the Monte Carlo sensitivity analysis are available in Supplementary Information S7. After 1000 simulations, results (Figure S7.1) showed a relative non-sensitivity to the estimate of parameters *b*, *S* and D_{84}, but a greater sensivity to the estimate of D_{50} . Yet, the value of 0.06 m for the D_{50} lies in the range that optimizes the transport capacity calculations. As such, the measurement of parameters *b*, *S*, D_{50} and D_{84} performed in this study appears appropriate with regards to transport capacity calculations, and with regards to the sensitivity of the parameters they are based upon.

In Figure 5d, the scatter around the trend line has up to three orders of magnitude of difference between the daily measured and predicted bedload mass for both over- and underestimation, which also emphasizes the limits of hydraulic-based estimates of bedload. Reasons for this discrepancy may be found in either erroneous estimates of the hydraulic forcing, or the temporally variable availability in sediment both at the bed and from the drainage network (e.g. sediment pulses; Elgueta-Astaburuaga et al., 2018). The density of data points below the 1:1 line in Figure 5d (particularly for smaller loads) may suggest that the shear stress-based equations tend on average to underestimate the transported bedload mass. Yet, the data points above the 1:1 line (i.e. overestimation of predicted bedload as compared to the measured one; logarithmic y-scale) have on average more weight when summing up daily values to annual loads, and largely compensate the underestimates of bedload at lower magnitude transport on a daily time-scale (Figure 5b).

3.2 Bedload transport, rainfall and the melt season

Bedload was summed for each year for “rain-forced” and “not rain-forced” days based on the classification of daily flow hydrographs (Figure 6a). Results show that a significantly greater proportion of annual bedload transport takes place during “rain-forced” daily flow hydrographs, as compared with “not rain-forced” daily flow hydrographs. On average over the five years of observation, ~86% of the annual bedload budget (75% to 91%) occurs during “rain-forced” daily flow hydrographs, while “not rain-forced” flow hydrographs (which notably include the melt-only signal) represent on average ~14 % of the annual bedload budget (9% to 25%). Note that “rain-forced” days may occur throughout the year, therefore they may be associated with a melt signal of varying intensity.

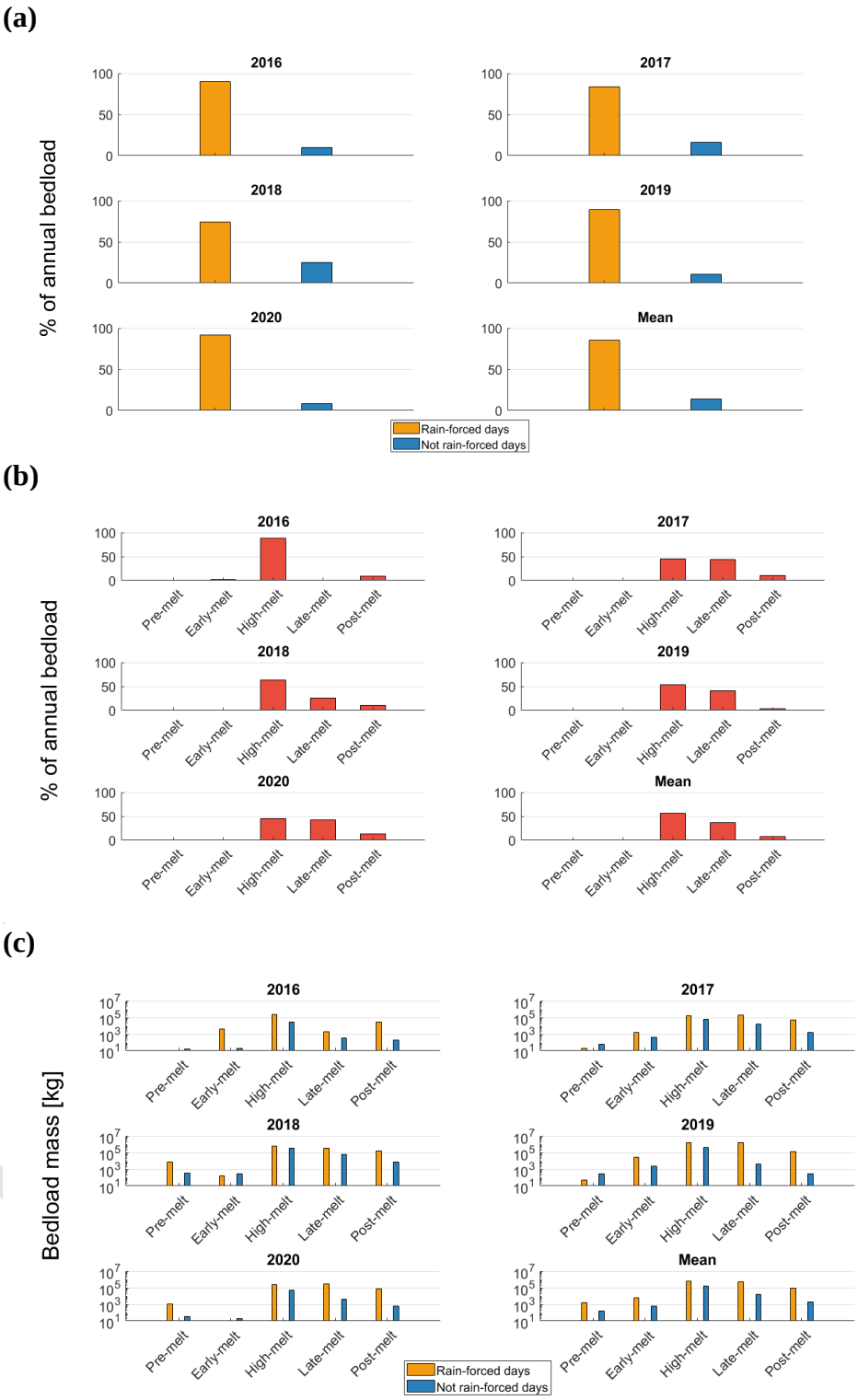

Figure 6. In (a), the proportion of annual bedload transport between "rain-forced" and "not rain-forced" days is presented for each of the five years of observation (2016-2020) and on average over the five years. In (b), the proportion of annual bedload transported for each of the five periods identified in flow hydrographs is presented (i.e. pre-melt, early-melt, high-melt, late-melt and post-melt) for each of the five years of observation and on average over the five years. In (c), total transported bedload mass per year and on average for each of the five periods, and between categories "rain-forced" and "not rain-forced" is presented. Note the logarithmic y-axes in Figure 6c.

Bedload transport was further summed by year for each of the five periods that have been identified based on the amplitudes of the daily flow hydrographs of "not rain-forced" days (Figure 6b). Results show that while the pre-melt and early-melt periods record no, or a negligible proportion (~ 1 %) of annual bedload, the high-melt season represents on average ~59 % (45% to 89 %) of the annual transported bedload. The late-melt period is the second period carrying the highest proportion of material, with on average ~31 % of the annual load (1-44 %), including year 2016 where a comparatively lower proportion of annual bedload was transported (1 %). The post-melt period was also responsible for a non-negligible part of the annual transported bedload, ~9 % on average (4% to 13 %). Note that each period contains both "rain-forced" and "not rain-forced" days.

Bedload was also investigated by combining the two categories, that is "rain-forced" and "not rain-forced" daily flow hydrographs, and the five periods with differing melt intensity (Figure 6c). Results show that the greatest masses of bedload are consistently transported during "rain-forced" days of the high-melt season throughout the five years of observation, representing on average ~47 % of the annual bedload. Then, the second highest volumes are transported during "rain-forced" days of the late-melt period, with an average of ~30 % of the annual bedload. In third place come "not rain-forced" days of the high-melt period, with an average of ~12 % of the annual bedload. Fourth place is occupied by "rain-forced" days of the post-melt season, with an average of ~9% of the annual bedload. The "not rain-forced" days of the late-melt season with an average of ~2% of the annual bedload is in fifth place. These are followed by the other categories, which carry a negligible proportion of the annual bedload transport (< 1 %).

3.3 Bedload transport magnitude-frequency

A progressive decline in the magnitude of daily bedload transport is observable with increasing frequency (expressed as a percentage of days), for both the total mass of bedload transported per day (Figure 7a), and for the daily maximum transport rate reached (Figure 7b).

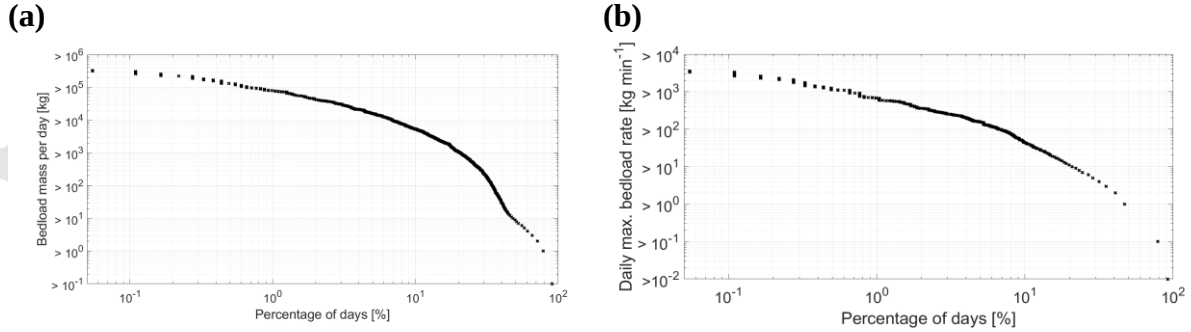

Figure 7. Magnitude-frequency relationship of daily bedload transport at the VdN throughout the five years of observation (2016-2020) for both (a) the daily bedload total mass transported and (b) the daily maximum transport rate reached.

The largest daily bedload total mass is $3.34 \cdot 10^5$ kg, while the highest daily maximum transport rate is $3.5 \cdot 10^3$ kg·min^{-1}. For ~0.6% of days (= 11 days) throughout the five years of observation daily bedload mass exceeds 10^5 kg; for ~0.6% of days, daily maximum rate is > 10^3 kg·min^{-1}. At intermediate magnitude-frequency, ~7% of days (= 128 days) have a daily bedload mass exceeds 10^4 kg, and ~7% of days when daily maximum rates are greater than 10^2 kg·min^{-1}. As magnitude further decreases (i.e. daily mass < 10^4 kg; daily peak rate < 10^2 kg·min^{-1}) and

frequency increases (> 128 days), there is a steep decline in the magnitude-frequency relationship for both variables (Figure 7).

Regarding the magnitude-frequency of "rain-forced" and "not rain-forced" days, "rain-forced" days appear to have daily bedload masses (Figure 8a) and daily maximum transport rates (Figure 8b) up to an order of magnitude greater than "not rain-forced" days for intermediate to low frequencies (< 10 % of days, 183 days). For instance, while the highest magnitude daily bedload mass of "rain-forced days" is $3.34 \cdot 10^5$ kg, the highest magnitude of "not rain-forced" days is $0.76 \cdot 10^5$ kg. Regarding daily maximum rates, the highest "rain-forced" transport rate is $3.5 \cdot 10^3$ kg·min^{-1}, while the highest "not rain-forced" peak rate is $0.58 \cdot 10^3$ kg·min^{-1}.

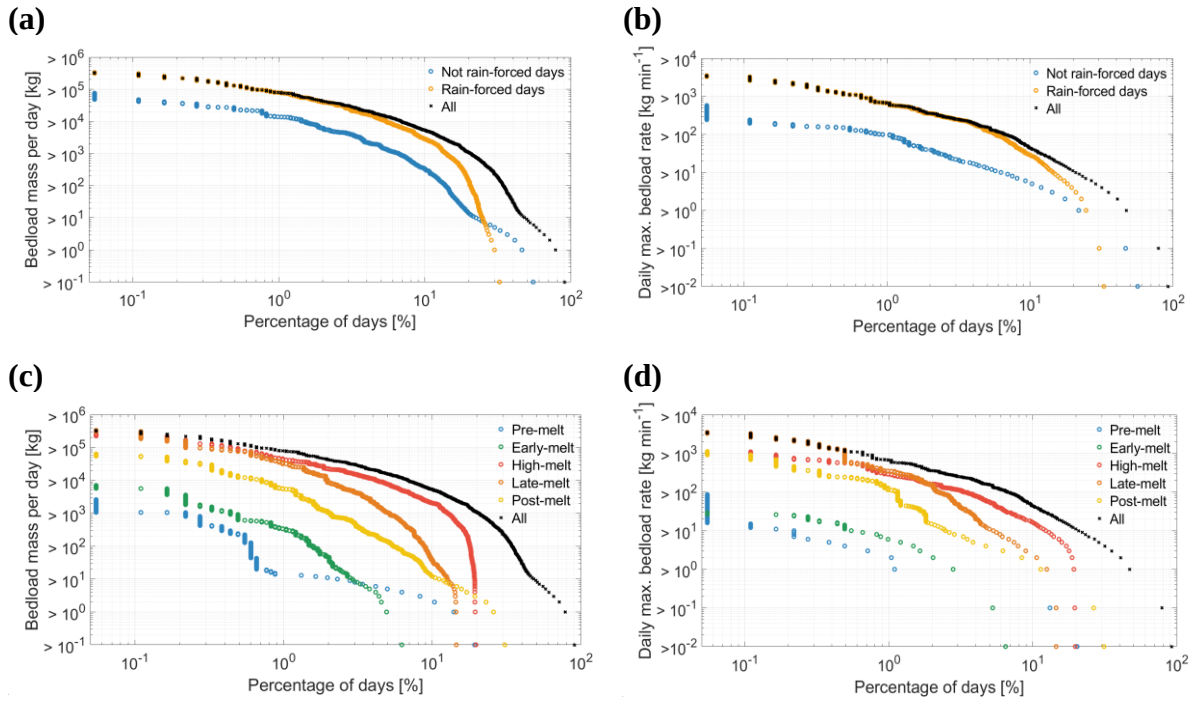

Figure 8. Magnitude-frequency relationship of daily bedload transport at the VdN between "rain-forced" and "not rain-forced" days for both (a) the daily bedload total mass transported and (b) the daily maximum transport rate reached, and between the five identified periods with differing melt intensity for both (c) the daily bedload total mass transported and (d) the daily maximum bedload rate reached.

By separating daily bedload transport between the five identified periods with differing melt intensity for both the daily bedload mass (Figure 8c) and the daily maximum transport rate (Figure 8d), the magnitude-frequency of daily bedload in the different periods of the melt season can be investigated. For daily bedload mass (Figure 8c), 0.6 % of days (= 11 days) with the highest magnitude bedload mass (> 10^5 kg) all occur during the high-melt and late-melt periods, followed by the post-melt period (10^4-10^5 kg), the early-melt (10^3-10^4 kg) and the pre-melt ($5 \cdot 10^2$-$3 \cdot 10^3$ kg) period. At intermediate to low frequencies (> 0.6 % of days), the high-melt period has the slowest decline in magnitude as the frequency increases. Magnitude decreases more rapidly in the other periods. Considering the daily maximum transport rate (Figure 8d), the late-melt period has the highest bedload rates (> $3 \cdot 10^3$ kg·min^{-1}), followed by the high-melt and post-melt periods (= $3 \cdot 10^3$ kg·min^{-1}), and then the early-melt and pre-melt periods (< 10^2 kg·min^{-1}). Similar to the daily bedload mass, the decline in the magnitude of daily maximum rates with increasing frequency is slower for the high-melt period than for other

periods, such that the late-melt period magnitude decreases to the same level as the high-melt period for frequencies of 0.5 – 2 % of days (= 9-37 days) and magnitudes of $0.2 \cdot 10^3$ -$1 \cdot 10^3$ kg·min^{-1}. At higher frequencies (> 2% of days) the high-melt period has the greatest daily maximum rate. The gap between the group "high-melt, late-melt, post-melt" and the group "early-melt, pre-melt" is more marked for the daily maximum transport rate magnitude-frequency relationships (Figure 8d) than those for the daily bedload mass (Figure 8c).

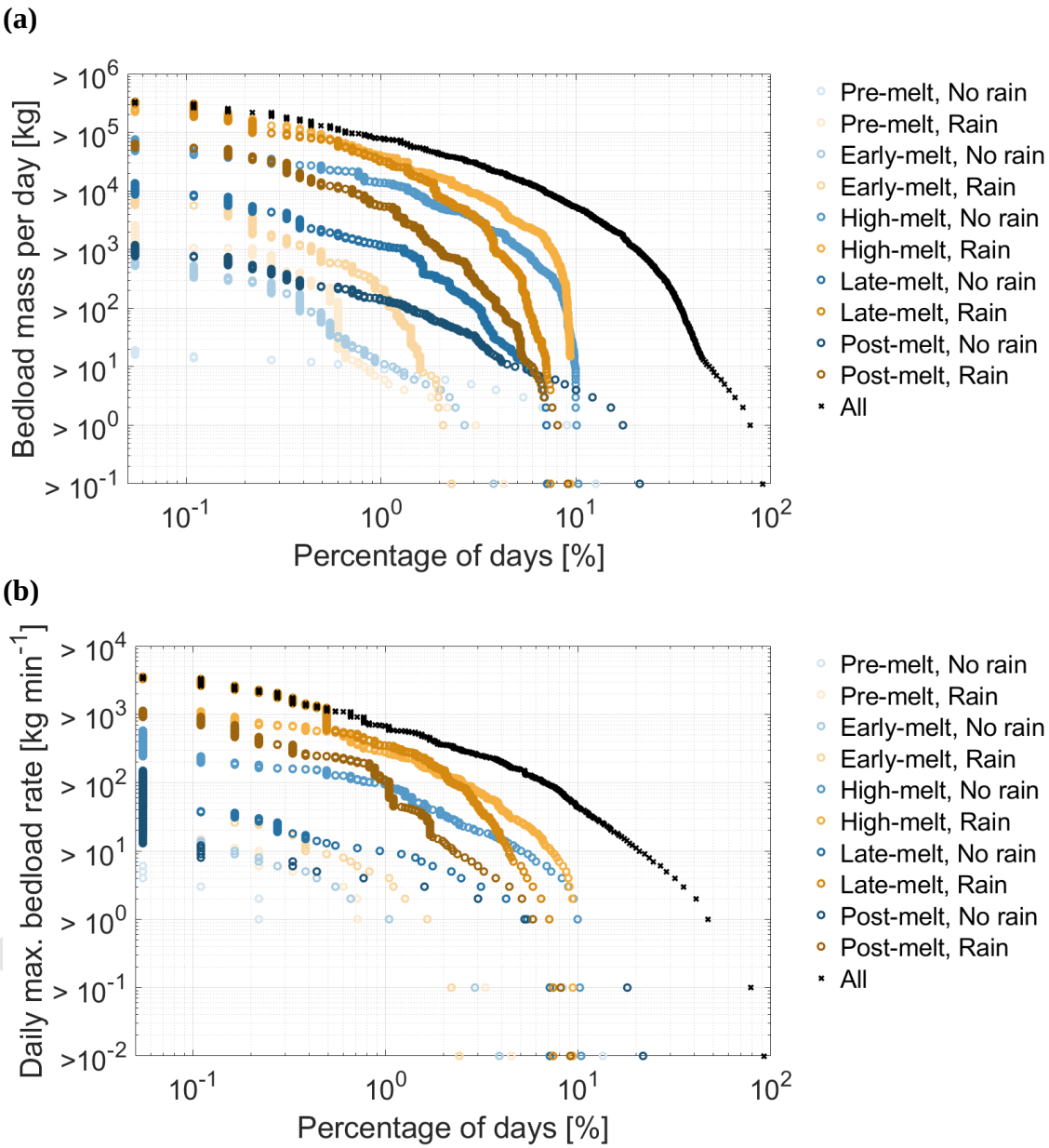

Figure 9. Magnitude-frequency relationship of daily bedload transport at the VdN between the five identified periods with differing melt intensity and between "rain-forced" days and "not rain-forced" days for both (a) the daily bedload total mass transported and (b) the daily bedload maximum transport rate reached.

In Figure 9, the magnitude-frequency relationships for daily bedload transport between "rain-forced" and "not rain-forced" days, and between the five periods with differing melt intensity, for both the daily bedload mass transported (Figure 9a) and the daily maximum transport rate reached (Figure 9b), are presented. For daily total mass (Figure 9a), at low frequencies (< 0.6 % of days, 11 days), high magnitudes (> 10^5 kg) are found during "rain-forced" days of the

high-melt and late-melt periods. Then come "rain-forced" days of the post-melt period and "not rain-forced" days of the high-melt period (10^4-10^5 kg), followed by "rain-forced" days of the early-melt and "not rain-forced" days of the late-melt period (10^3-10^4 kg). "Rain-forced" days of the pre-melt period, and "not rain-forced" days of the post-melt, early-melt and pre-melt periods all record relatively low bedload magnitudes (< 10^3 kg), even at these low frequencies of occurrence. At intermediate frequencies (0.6-2% of days, 11-37 days), the highest magnitudes are recorded for, in decreasing order: "Rain-forced – high-melt"; "Rain-forced – late-melt"; "Not rain-forced – high-melt"; "Rain-forced – post-melt"; "Not rain-forced – late-melt"; followed by the other categories, which carry less substantial masses of bedload. At high frequencies (> 2%), the magnitude of the pair "Rain-forced – Late-melt" days decrease more rapidly than the pairs "Rain-forced – High-melt" and "Not Rain-forced – High-melt".

Regarding daily maximum transport rates (Figure 9b), for low frequencies (< 0.6 % of days, 11 days), the highest bedload intensity (> $3 \cdot 10^3$ kg·min^{-1}) is associated with "rain-forced" days of the late-melt period, followed by "rain-forced" days of the high-melt period, "rain-forced" days of the post-melt period, "not rain-forced" days of the high-melt period and "not rain-forced" days of the late-melt period, followed by the other categories. At intermediate frequencies (0.6-2 % of days, 11-37 days), the highest bedload intensities are found in "rain-forced" days of the high-melt and late-melt periods, followed by "rain-forced" days of the post-melt period, and "not rain-forced" days of the high-melt period, followed by the other categories. At high frequencies (> 2%), the magnitude of the pair "Rain-forced – Late-melt" days decrease more rapidly than the pairs "Rain-forced – High-melt" and "Not Rain-forced – High-melt". The magnitude-frequency of daily bedload transport for each year separately integrated over the different hydrological categories developed in this paper is available in Supplementary Information S8.

4. Discussion

4.1 Annual bedload masses and their variability

Average annual erosion rates estimated from bedload transport export at the VdN can be compared with other Alpine watersheds where bedload data have been reported. To make the inter-basin comparison appropriate, we only selected headwater watersheds that are between 5 and 85 km^2 in size, and with a glaciated area < 40%. These two variables, together with associated annual transport capacity, channel gradient and the geological setting, were shown to considerably affect annual bedload export (Hinderer et al., 2013; Lauffer and Sommer, 1982; Rickenmann, 2020, 2012, 1997; Spreafico and Lehmann, 1994; Turowski et al., 2010). Details of the watersheds presented in Figure 10 are available in Supplementary Information S9 (Table S9.1), with the associated references.

With an average of 0.039 mm·y^{-1}, the VdN is a relatively active watershed in terms of bedload export as compared with other reported Alpine watersheds (Figure 10), both glaciated and unglaciated. The VdN (3 % glaciated) has comparable erosion rates to some watersheds that are more glaciated, such as the Fischbach (16%), the Ruetz (20%), the Minstigerbach (20%) and the Lonza (37 %), but lower erosion rates than more active watersheds such as the Haut Glacier d'Arolla (27%) or the Val Roseg (30%) (FOEN, 2010; Lane et al., 2017; Rickenmann, 2018; Spreafico and Lehmann, 1994; Tockner et al., 2002; Figure 10). These comparisons are however complicated by the basin Sediment Delivery Ratio (SDR) which commonly decreases with increasing watershed area, reflecting that larger basins store more material than smaller

ones (e.g. Hinderer et al., 2013), and that specific bedload transport capacities (per unit watershed area) decrease due to decreasing channel steepness (Rickenmann and Koschni, 2010).

When looking at the inter-annual variability in exported bedload over the five years investigated, the VdN has a factor of 10 difference between the least (2016) and the most (2019) active year (Figure 5b). This is more than reported for the Fischbach and the Ruetz basins, where ~10 years of monitoring suggest a factor 4.5 and 5 between the least and the most active year, respectively (Rickenmann, 2018; Rickenmann et al., 2020). The factor is less than reported for the Rio Cordon, where annual loads between 0 and $1.5 \cdot 10^6$ kg have been observed over three-decades of survey (Rainato et al., 2017). Inter-annual differences may reflect mean annual temperatures, the annual quantity of precipitation (both snowfall and rainfall), and/or the time-integrated shear stress, although our results suggest no simple systematic relationships between bedload export and such variables, Of greater importance may be the intensity and timing of the hydrological events taking place (e.g. watershed snow content, timing and magnitude of the melt, timing and magnitude of rainfall, baseflow intensity; Figure 5, 6, 8, 9), and also changes in sediment availability.

(a)

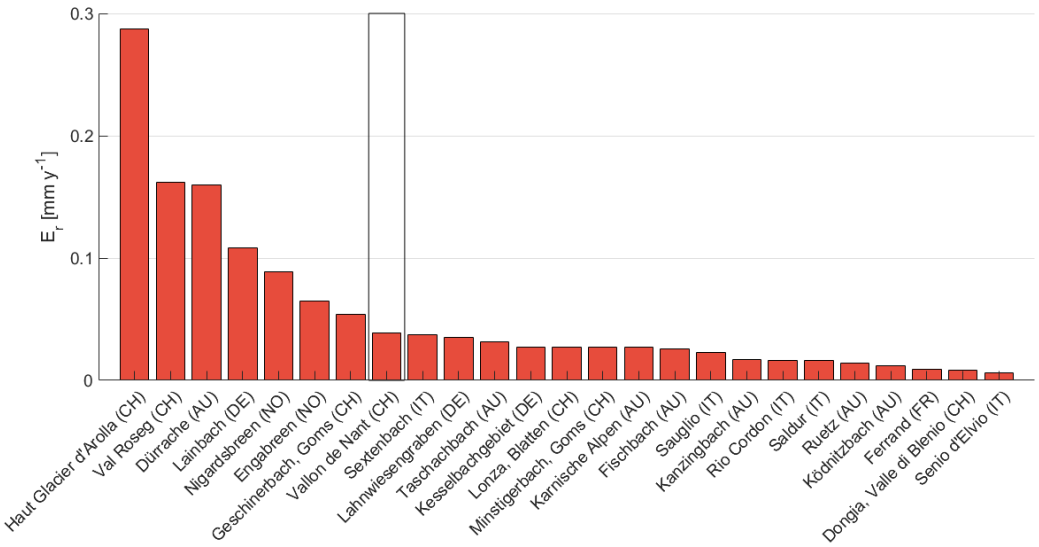

Figure 10. (a) Erosion rates calculated from exported bedload at multiple headwater Alpine watersheds with comparable area and glacier cover as the VdN. The VdN is highlighted with a black box.

4.2 Hydraulic forcing and bedload transport

The prediction of bedload transport using shear stress-based (i.e. transport capacity) equations has emphasized the importance of hydraulic forcing of bedload transport (Figure 5a, 5b, 5d). The relationship between the measured and predicted daily bedload mass (Figure 5d), is notably in general agreement with the 1:1 line, and with previous research, which used the same modified form of the Wilcock and Crowe (2003) equations to compare measured and predicted bedload mass (e.g. Rickenmann, 2020; Rickenmann et al., 2020; Schneider et al., 2015).

Although it is clear that the hydraulic forcing is of importance, the considerable overestimation of the predicted annual bedload as compared to the annual measured bedload (Figure 5b), and

the considerable scatter in the relationship between daily measured bedload mass and predicted daily bedload mass (Figure 5d), illustrates the importance of other drivers of bedload transport rate. A poor representation of hydraulics near the bed in the driving equations of bedload, in particular around the threshold of motion, represents one set of uncertainties around shear stress-based estimates of bedload transport (e.g. Buffington and Montgomery, 1997; Gomez, 1991). In addition, temporal changes in sediment availability, both as a function of bed material mobility (i.e. bedload pulses; Elgueta-Astaburuaga et al., 2018), and as a function of sediment supply from the drainage network (i.e. "travelling bedload"; Piton and Recking, 2017), is another dimension of bedload transport that is poorly covered by capacity-based transport equations (e.g. Rickenmann, 2020). Because the VdN system is likely to oscillate between capacity-limited and supply-limited conditions, the same hydraulic forcing is not expected to systematically induce the same amount of bedload, and this discrepancy is notably visible in the general overestimation of bedload masses at the VdN when applying the transport capacity-based equations (equations [6-10]; Figure 5b).

Many studies have attempted to assess changes in streambed state and associated sediment mobility. Flood regime history in terms of magnitude-frequency was notably found to be an important factor regarding bed armoring cycles and associated sediment mobility (Mao, 2018; Masteller et al., 2019; Rickenmann, 2020). Also, the infiltration of fine material into the bed matrix was also hypothesized as an important control on bed sediment mobility (e.g. An et al., 2019; Venditti et al., 2010). Some research has also attempted to identify potential seasonal trends in sediment availability within Alpine watersheds. Mao et al. (2014) have for instance related the direction of hysteresis loops between streamflow and bedload transport rates to seasonal change in sediment supply from the drainage network. Yet, the balance between bed state and supply from the drainage network in terms of sediment production could not be partitioned. Therefore, the extent to which sediment availability changes through time, and how it affects the relationship between streamflow and bedload transport, remains poorly constrained (Elgueta-Astaburuaga and Hassan, 2019; Reid et al., 2019; Rickenmann, 2020). Sediment availability being a complex variable to quantify, a possible approach for future research could be based upon probabilistic estimate of bedload according to the hydrological conditions met in a given Alpine watershed. For instance, the results of this study have shown the higher probability of having large bedload transport events during rainy days occurring when the melt signal is strong and baseflow is high, which could reflect both hydraulic forcing and sediment availability conditions, as well as higher particle velocity and sediment connectivity throughout the watershed (e.g. Dell'Agnese et al., 2015). Future research should focus on obtaining distributed estimates of bedload flux to properly quantify change in sediment availability, and its effect on the streamflow-bedload relationship. This could be performed either through the deployment of a network of passive bedload sensors (e.g. Cook et al., 2018; Misset et al., 2021), or through repeated topographical surveys at high spatial and temporal resolutions (e. g. Antoniazza et al., 2019; Bakker et al., 2019; Dai et al., 2021; James et al., 2020).

4.3 Magnitude-frequency of daily bedload transport during rainfall and the melt season

The approach adopted in this paper allows, for the first time, the comparison of a relatively long-term continuous time-series of bedload export with the hydrological patterns of an Alpine watershed. The visual inspection of 1827 daily flow hydrographs, supported with temperature and precipitation datasets, permitted distinction of daily flow hydrographs influenced by

rainfall from the ones that were not. The amplitude of daily flow hydrographs of "not rain-forced" days (Mutzner et al., 2015) was further used to identify five periods with differing melt intensity – the pre-melt, early-melt, high-melt, late-melt and post-melt periods – that were recurrently met throughout the five years of observation on the one hand, and which varied within a same range of discharge amplitude on the other hand (Figure 4; Table 1).

The results of this study show that the largest quantities of bedload export were associated with a combined occurrence of rainfall at times when baseflow is high and when the snowmelt signal is strong (Figure 6, Figure 8, Figure 9). This concerns both the total amount of bedload transported, and the maximum bedload transport rate reached. At this period of the year, the lower and/or exposed parts of the watershed have already lost snow cover, reducing the storage capacity of the snowpack and exposing more sediment. At higher elevations and/or in sheltered areas of the watershed, large volumes of snow may still be available. Melt has commonly started and subsurface water storage is typically high in the lower parts of the watershed, which is visible in the high baseflow in these periods (Figure 5a). When rain occurs in such conditions, the remaining snow cover may provide additional rapid melt but only little additional water storage capacity for incoming water inputs, and significant surface runoff is produced. As the subsurface may already be saturated due to melt and percolation through the snowpack and infiltration into the soil, little incoming water can be absorbed (Corripio and López-Moreno, 2017; Li et al., 2019; Musselman et al., 2018), and a rapid increase in the streamflow hydrograph is expected, favorable to sediment mobilization and bedload transport. In addition, the extension of the stream network (Michelon et al., 2021) may access new sedimentary sources. In comparison, incoming rain occurring earlier in the year (e.g. pre-melt and early-melt period; Figure 6, Figure 8, Figure 9), when the snowpack is colder, more extensive and deeper, can be at least partly stored within the snowpack or in the underlying soil, thus producing a comparatively smaller streamflow response. Retraction of the stream network during this period (Michelon et al., 2021) also reduces the access to sedimentary sources. Under such conditions, little bedload is transported.

Rainfall occurring later in the year, once the watershed snow water equivalent has decreased and the melt signal is not as strong anymore (e.g. post-melt period), can also produce significant amounts of bedload, but to a lesser extent than rainfall occurring during the high-melt and late-melt periods (for both total bedload per day and daily maximum transport rate), notably because the baseflow is lower (Figure 5a). Intense summer and autumn storms are expected to produce rapid streamflow response and increase bedload transport capacity (e.g. Rainato et al., 2017; Rickenmann, 2020). Those events can produce high transport capacity discharge and bedload transport events (both in terms of total bedload and daily maximum transport rate). However, their magnitude decreases much more rapidly with increasing frequency than for bedload transported during the high-melt and late-melt season (for both "rain-forced" and "not rain-forced" days; Figure 6, Figure 8, Figure 9), again due to lower baseflow at this period of the year. This means that whilst rainfall events of the post-melt season matter for low-frequency high-magnitude events, their role in terms of annual total bedload transported seems less important. Whilst "rain-forced" days dominate the bedload signal at all magnitude-frequency combinations, snowmelt events alone is still capable of transporting a substantial amount of bedload during the high-melt and late-melt periods (Figure 6, Figure 8, Figure 9), when the baseflow is higher.

The dataset to which the observation made in this paper can be best compared is the study of Rainato et al. (2017). The authors investigated the magnitude-frequency of bedload transport events over three decades at the Rio Cordon Alpine watershed (Italian Alps), which was shown to deliver comparable annual bedload yields to the VdN (Figure 10). Over the 31 bedload transport events recorded during the period 1986-2014, a slight majority of them (17) occurred during the period when snow was still (or already) likely present within the watershed (e.g. May-June; November). Yet, a substantial proportion of bedload transport events (14) also took place when the likelihood of having considerable remaining snow had decreased (e.g. July-October). Therefore, the imbalance between bedload transport occurring during the melt season (including rainy days of the melt season), and bedload transport occurring during rainfall once the watershed snow content has significantly decreased, seems to be greater at the VdN as compared with the Rio Cordon. This may be due to particularly intense rainfall during the late summer and autumn at the Rio Cordon, combined with changes in the connectivity of sedimentary sources through the season (Rainato et al., 2017). However, with no complete hydrological study (e.g. melt signal, rainfall versus melt-driven bedload transport) of the events producing bedload at the Rio Cordon, a direct comparison with the categories developed in this paper remains difficult.

4.4. Bedload transport perspectives under climate change

The dataset presented in this paper shows the importance of the seasonal timing of hydrological drivers for triggering bedload transport, where the seasonal timing is a proxy for the extension of the stream network (Michelon et al., 2021), for the baseflow level and for the strength of the melt signal. These results are of importance in the perspective of understanding how bedload transport in Alpine watersheds may evolve with climate change, because the latter is likely to affect both the timing of occurrence and the magnitude of the bedload-driving hydrological events.

A summary of the meteorological, hydrological and bedload transport patterns highlighted over the five years of observation at the VdN, and projections on how these variables could evolve with climate change, is provided in Figure 11. Current mean temperature, rainfall and snowfall have been estimated with the RhiresD and TabsD datasets over the period 2016-2020. Discharge and bedload data come from the VdN monitoring station. Rough projections of mean temperature, rainfall, snowfall and baseflow for the end of the 21th century (2085) for the Western Alps were performed using the datasets presented in CH2018 (2018) and FOEN (2021) for the RCP4.5 scenario (i.e. moderate warming). Under this scenario, mean temperatures are projected to rise for all seasons, especially in summer, while mean snowfall should decrease for all seasons, notably in spring and autumn. Mean rainfall is project to decrease in the summer, and rise in the other seasons, notably in winter (CH2018, 2018; FOEN, 2021; Figure 11). The intensity of extreme precipitation events in all seasons is expected to follow the increase that is already observed. Increase in intensity is estimated to be about +20% in magnitude by the end of the century, for both hourly events and multi-day events (CH2018, 2018).

The impacts of these general climatic trends on high Alpine water resources have long been known (Horton et al., 2006). These impacts are largely related to the evolution of the seasonal snow line (i.e. the average elevation at which snow falls), which is expected to rise by between 300 m and 600 m by the end of the 21th century (CH2018, 2018). Indeed, the wintertime increase in precipitation is projected to not be able to compensate the large loss in snow volume caused

by the increase in temperature, except at very high elevations (FOEN, 2021). Less precipitation will thus be stored as snow and the formation of a seasonal snow cover will occur later in the year, with a shift in maximum snow heights from March to February (CH2018, 2018). Snowmelt is projected to occur earlier in the year, leading to significant shifts of the seasonal streamflow regimes of high elevation watersheds (CH2018, 2018; FOEN, 2021). Groundwater recharge is also expected to evolve with climate change, with an increase of groundwater recharge in winter and spring, and a decrease in summer and autumn, which is of importance to determine change in baseflow (FOEN, 2021).

As a consequence of these changes, the hydrological regime of currently snow-dominated Alpine watersheds such as the VdN is expected to shift to a more rain-influenced streamflow regime by the end of the 21st century, with less snow accumulation, with gentler and earlier snowmelt, and with a monthly streamflow maximum occurring earlier in the year (FOEN, 2021). This will namely result in a marked increase of winter streamflow (+ 80-100%), a moderate increase in spring streamflow (+ 20-40%), a marked decrease in summer streamflow (-40 to -60%), and a moderate decrease in autumn streamflow (FOEN, 2021). Yet, mean annual streamflow is expected to remain generally stable, or to decrease slightly (FOEN, 2021). Regarding high streamflow events, no detailed climate-model based projections are currently available for Alpine water resources at catchment-scale because the CH2018 climate scenarios have not been yet downscaled for hydrological purposes to local Alpine conditions.

How could bedload transport evolve together with changes in the hydrological drivers within snowmelt-dominated Alpine watersheds? The increase in the magnitude and frequency of extreme precipitation events, and in the associated magnitude and frequency of high streamflows, has led some researchers to argue for a probable increase in the amount of bedload that will be transported under climate change conditions (CH2018, 2018; FOEN, 2021; Speerli et al., 2020). However, these predictions do not take into account possible change in the hydrological drivers responsible for bedload transport, and this statement can be challenged, to some extent, by the results presented in this paper.

From a hydrological regime shift perspective, the periods of high-melt and late-melt will occur earlier in the year, at lower baseflow (i.e. resulting from a reduced winter snowpack). This shift to earlier periods in the year might reduce the daily melt amplitude because the melt period is shifted to colder periods of the year (Musselman et al., 2017). Accordingly, the contribution of the melt-only events to bedload transport, especially important during the high-melt and late-melt periods, is likely to decrease together with annual snow volumes, due to the combined effect of lowered baseflow and lowered daily flow amplitudes. The results here show that while it may not affect significantly transport maxima, it may be of importance regarding annual bedload totals (Figure 6, Figure 8, Figure 9).

Translating these changes into meteorological spring and summer periods, we can expect the amount of bedload transport throughout the spring to rise, while the amount of bedload transported throughout the summer can be expected to decrease. A central question that needs to be addressed is whether the importance of the combined occurrence of heavy rainfall over a watershed where the melt signal is strong and baseflow is high – as occurs currently especially during summer – will be maintained with climate change, or whether a disconnection between the high-melt and late-melt periods and the projected occurrence of heavy rainfall may take

place under climate change conditions. If the latter situation occurs, a decrease in the bedload contribution of rain events during the high-melt and late-melt periods is possible in the future.

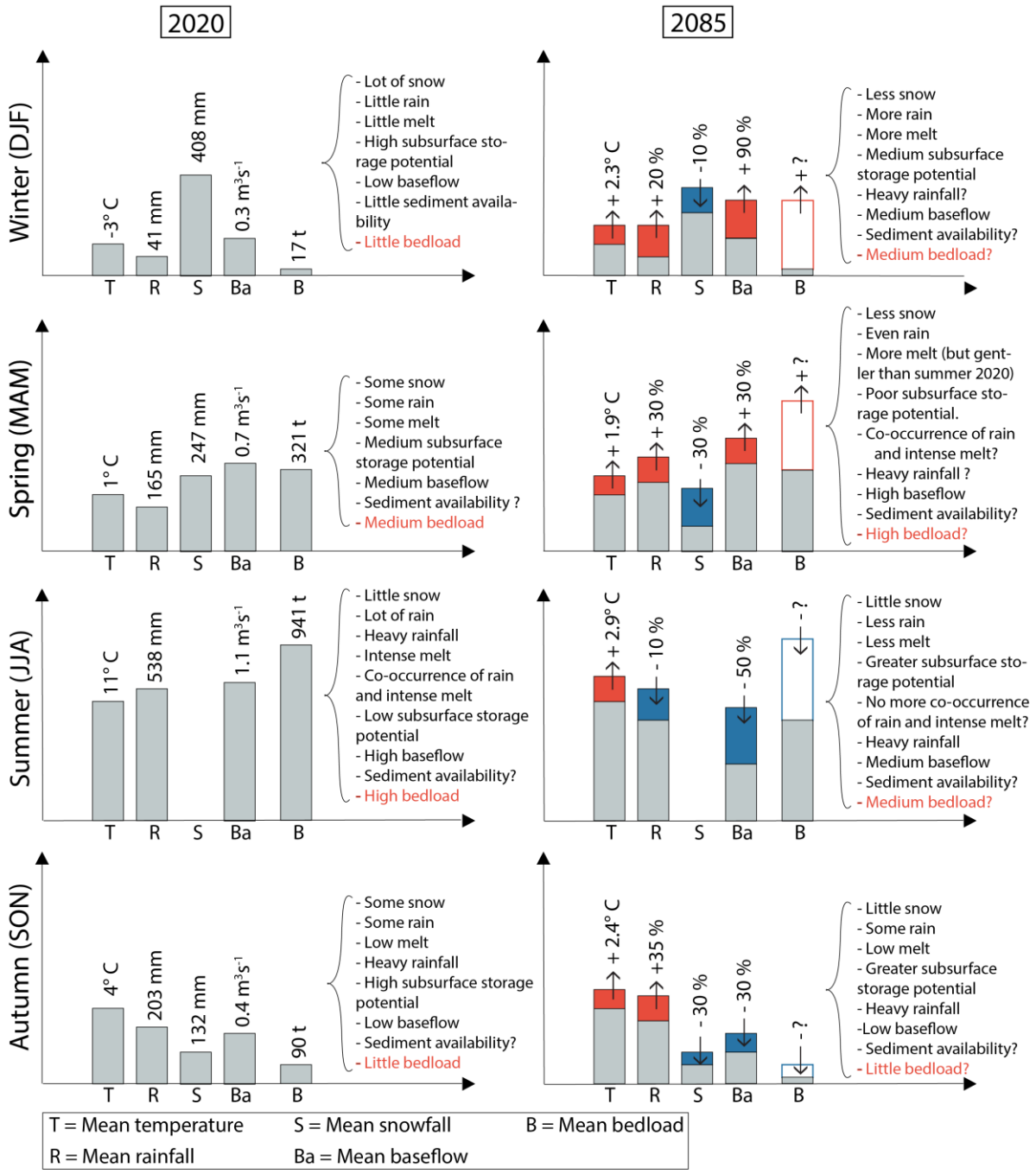

Figure 11. Summary of the meteorological, hydrological and bedload transport patterns observed at the VdN (left panels) over the period 2016-2020. Projections on possible evolutions, and main uncertainties to solve regarding seasonal change in bedload transport with climate change (right panels).

Another central question regards how the predicted increase in winter rainfall and winter streamflow will impact bedload transport. This general increase of liquid water availability in winter will most likely increase winter bedload transport, but the question of the magnitude of

the increase is key. During winter rainfall events within watersheds that continue to show a significant seasonal snow cover, the incoming water may be stored to some extent, filtering out the streamflow and bedload response, as it is visible for current rainfall taking place during the pre-melt and early-melt periods. Thus, the response of any one watershed to winter warming and the occurrence of winter rainfall is likely to depend on its hypsometry (CH2018, 2018).

The last central question regards the increase in heavy rainfall throughout the year. Given that high-magnitude bedload transport events were shown to occur following heavy rainfall events, their timing of occurrence, notably with regards to the co-occurrence with high melt intensity or with high baseflow, may matter to determine the magnitude of the answer of streamflow and bedload transport. It is therefore of great importance to quantify the extent to which the increase in magnitude and frequency of rainfall will affect both maximum values of bedload transport rates and annual bedload export, and whether these events will have the capacity of compensating and/or overcoming reductions of bedload transport that may take place during other periods of the year.

Estimates of the evolution of bedload transport under climate change conditions need also to include expected changes in sediment availability within Alpine watersheds, because the latter matters to determine actual sediment export, whatever transport capacity the streams reach (Lane et al., 2017; Lane and Nienow, 2019; Figure 10). Sediment availability is also expected to change together with climate change, but the sign of the trend remains uncertain. On the one hand, permafrost degradation is thought to increase sediment supply from rockwalls and rockslopes (Messenzehl et al., 2018; Ravanel and Deline, 2011), and glacier retreat increases the volume of unstabilized easily-remobilizable material (e.g. Antoniazza and Lane, 2021; Ballantyne, 2002; Carrivick and Heckmann, 2017; Lane et al., 2017; Mancini and Lane, 2020). Also, the increase in magnitude and frequency of rainfall may increase the frequency of debris flows (e.g. Stoffel et al., 2014) and landslides (Huggel et al., 2012). On the other hand, the effects of climate change may also reduce sediment production, and associated processes (e.g. debris flow) by negative feedbacks such as due to the reduction in the frequency of frost-thaw cycles (e.g. Hirschberg et al., 2021). Similarly, the sustained paraglacial adjustment of Alpine watersheds following the Little Ice Age is thought to lead to the progressive stabilization of glacially-conditioned material (e.g. Antoniazza and Lane, 2021; Ballantyne, 2002; Porter et al., 2019) and to a disruption of sediment connectivity within Alpine watersheds (Lane et al., 2017; Mancini and Lane, 2020; Micheletti et al., 2015; Micheletti and Lane, 2016), which may cause a progressive decrease in sediment transfer. In this context, a critical uncertainty remains to know whether sediment connectivity could also be sustainably enhanced by the increase in the magnitude and frequency of heavy rainfall and high flows (Cossart and Fort, 2008; Porter et al., 2019); or decreased due to feedbacks associated with landscape adjustment to climate change.

5. Conclusion

This paper presents a five-year time-series (2016-2020) of bedload transport monitored with the Swiss Plate Geophone (SPG) system at the VdN Alpine watershed, in the Western Swiss Alps. The analysis of five years of observation shows the importance of the co-occurrence of rainfall with a strong snowmelt signal and/or a high baseflow for producing frequently high-magnitude and intermediate-magnitude bedload transport. High-magnitude low-frequency bedload transport is also shown to occur when the melt signal is much weaker in the presence

of rainfall, but the magnitude-frequency of daily bedload masses declines much quicker than when the melt signal is still strong due to lower baseflow. Although rainfall seems to represent the dominant driver of bedload transport (both during and after the snowmelt period), bedload transport can also be caused by the melt-only events. The latter contributes more by proportion to bedload totals, than to maximum transport rates. The analysis also shows the importance of sediment availability in influencing the relationship between streamflow and bedload transport, which requires more attention within future research.

There are concerns that bedload transport in Alpine watershed may increase associated with the magnitude and frequency of rainfall-induced high stream flows. However, the results of this study show that the timing and co-occurrence of hydrological drivers (i.e. rainfall, melt, baseflow) matters in determining the magnitude and frequency of bedload transport. As such, it is not clear yet how those elements and their temporal interplay will evolve under climate change conditions.

6. Acknowledgements

The authors thank the University of Lausanne for supporting this work. The University of Lausanne, the Swiss Federal Research Institute WSL and the Physics of Environmental Systems group of the ETH Zürich are further thanked for financing the building of the monitoring station at the VdN. The calibration of the SPG system at the VdN was partly supported by the Swiss National Science Foundation SNSF (grant 200021L_172606 awarded to DR). The authors are grateful to Mehdi Mattou, Nicolas Steeb, Florian Schläfli and Konrad Eppel for their great help for the collection of the bedload samples that were used to calibrate the SPG. Magalí Matteodo, Thomas Antoniazza, Aurélien Ballu, Matteo Roncoroni, Dilan Reich, Jens Turowski and Eduardo Viegas are further thanked for their help in the field and/or for their suggestions regarding the elaboration of this work. Francesco Comiti and another anonymous reviewer are thanked for their valuable comments on earlier versions of this manuscript.

Conflict of interest statement

The authors declare no conflict of interest.

Data availability statement

All data presented in this paper will be made available online on the EnviDat repository https://www.envidat.ch/#/metadata/sediment-transport-observations-in-swiss-mountain-streams upon publication of the manuscript.

7. References

An, C., Parker, G., Hassan, M.A., Fu, X., 2019. Can magic sand cause massive degradation of a gravel-bed river at the decadal scale? Shi- ting River, China. Geomorphology 327, 147–158. https://doi.org/10.1016/j.geomorph.2018.10.026

Ancey, C., 2020a. Bedload transport: a walk between randomness and determinism. Part 1. The state of the art. Journal of Hydraulic Research 58, 1–17.

Ancey, C., 2020b. Bedload transport: a walk between randomness and determinism. Part 2. Challenges and prospects. Journal of Hydraulic Research 58, 18–33.

Antoniazza, G., Bakker, M., Lane, S.N., 2019. Revisiting the morphological method in two-dimensions to quantify bed-material transport in braided rivers. Earth Surface Processes and Landforms 44, 2251–2267. https://doi.org/10.1002/esp.4633

Antoniazza, G., Lane, S.N., 2021. Sediment yield over glacial cycles: A conceptual model. Progress in Physical Geography: Earth and Environment 0309133321997292. https://doi.org/10.1177/0309133321997292

Antoniazza, G., Nicollier, T., Wyss, C.R., Boss, S., Rickenmann, D., 2020. Bedload Transport Monitoring in Alpine Rivers: Variability in Swiss Plate Geophone Response. Sensors 20, 4089. https://doi.org/10.3390/s20154089

Ashworth, P.J., Ferguson, R.I., 1986. Interrelationships of channel processes, changes and sediments in a proglacial braided river. Geografiska Annaler: Series A, Physical Geography 68, 361–371.

Badoux, A., Andres, N., Techel, F., Hegg, C., 2016. Natural hazard fatalities in Switzerland from 1946 to 2015. Natural Hazards and Earth System Sciences 16, 2747–2768.

Badoux, A., Andres, N., Turowski, J., 2014a. Damage costs due to bedload transport processes in Switzerland. Natural Hazards and Earth System Sciences 14, 279–294. https://doi.org/10.5194/nhess-14-279-2014

Badoux, A., Peter, A., Rickenmann, D., Junker, J., Heimann, F., Zappa, M., Turowski, J.M., 2014b. Geschiebetransport und Forellenhabitate in Gebirgsflüssen der Schweiz: mögliche Auswirkungen der Klimaänderung. Wasser Energie Luft 106, 200–209.

Bakker, M., Antoniazza, G., Odermatt, E., Lane, S.N., 2019. Morphological Response of an Alpine Braided Reach to Sediment-Laden Flow Events. Journal of Geophysical Research: Earth Surface 124, 1310–1328. https://doi.org/10.1029/2018JF004811

Ballantyne, C.K., 2002. Paraglacial geomorphology. Quaternary Science Reviews 21, 1935–2017. https://doi.org/10.1016/S0277-3791(02)00005-7

Barton, J.S., Slingerland, R.L., Pittman, S., Gabrielson, T.B., 2010. Monitoring coarse bedload transport with passive acoustic instrumentation: A field study. US Geol. Surv. Sci. Invest. Rep 5091, 38–51.

Bollrich, G., 2000. Technische Hydromechanik 1, 5. Auflage. Verlag Bauwesen, Berlin.

Buffington, J.M., Montgomery, D.R., 1997. A systematic analysis of eight decades of incipient motion studies, with special reference to gravel- bedded rivers. Water Resources Research 33, 1993–2029.

Bunte, K., Abt, S.R., 2005. Effect of sampling time on measured gravel bed load transport rates in a coarse- bedded stream. Water Resources Research 41.

Bunte, K., Abt Steven R., Potyondy John P., Ryan Sandra E., 2004. Measurement of Coarse Gravel and Cobble Transport Using Portable Bedload Traps. Journal of Hydraulic Engineering 130, 879–893. https://doi.org/10.1061/(ASCE)0733-9429(2004)130:9(879)

Burtin, A., Bollinger, L., Vergne, J., Cattin, R., Nábělek, J.L., 2008. Spectral analysis of seismic noise induced by rivers: A new tool to monitor spatiotemporal changes in stream hydrodynamics. Journal of Geophysical Research: Solid Earth 113. https://doi.org/10.1029/2007JB005034

Carrivick, J.L., Heckmann, T., 2017. Short-term geomorphological evolution of proglacial systems. Geomorphology, Sediment cascades in cold climate geosystems 287, 3–28. https://doi.org/10.1016/j.geomorph.2017.01.037

Ceperley, N., Michelon, A., Escoffier, N., Mayoraz, G., Boix Canadell, M., Horgby, A., Hammer, F., Antoniazza, G., Schaefli, B., Lane, S., Rickenmann, D., Boss, S., 2018. Salt Gauging And Stage-Discharge Curve, Avançon De Nant, Outlet Vallon De Nant Catchment. https://doi.org/10.5281/zenodo.1154798. Version V1.0.0 [Data set]. Zenodo.

Ceperley, N., Zuecco, G., Beria, H., Carturan, L., Michelon, A., Penna, D., Larsen, J., Schaefli, B., 2020. Seasonal snow cover decreases young water fractions in high Alpine catchments. Hydrological Processes 34, 4794–4813. https://doi.org/10.1002/hyp.13937

CH2018, 2018. CH2018 - Climate Scenarios for Switzerland, Technical Report. National CEntre for Cliamte Services, Zürich.

Comiti, F., Mao, L., Penna, D., Dell'Agnese, A., Engel, M., Rathburn, S., Cavalli, M., 2019. Glacier melt runoff controls bedload transport in Alpine catchments. Earth and Planetary Science Letters 520, 77–86. https://doi.org/10.1016/j.epsl.2019.05.031

Cook, K.L., Andermann, C., Gimbert, F., Adhikari, B.R., Hovius, N., 2018. Glacial lake outburst floods as drivers of fluvial erosion in the Himalaya. Science 362, 53–57. https://doi.org/10.1126/science.aat4981

Corripio, J.G., López-Moreno, J.I., 2017. Analysis and Predictability of the Hydrological Response of Mountain Catchments to Heavy Rain on Snow Events: A Case Study in the Spanish Pyrenees. Hydrology 4, 20. https://doi.org/10.3390/hydrology4020020

Cossart, E., Fort, M., 2008. Sediment release and storage in early deglaciated areas: Towards an application of the exhaustion model from the case of Massif des Écrins (French Alps) since the Little Ice Age. Norsk Geografisk Tidsskrift - Norwegian Journal of Geography 62, 115–131. https://doi.org/10.1080/00291950802095145

Dai, W., Xiong, L., Antoniazza, G., Tang, G., Lane, S.N., 2021. Quantifying the spatial distribution of sediment transport in an experimental gully system using the morphological method. Earth Surface Processes and Landforms 46, 1188–1208. https://doi.org/10.1002/esp.5094

Dell'Agnese, A., Brardinoni, F., Toro, M., Mao, L., Engel, M., Comiti, F., 2015. Bedload transport in a formerly glaciated mountain catchment constrained by particle tracking. Earth Surface Dynamics 3, 527–542. https://doi.org/10.5194/esurf-3-527-2015

Dell'Agnese, A., Mao, L., Comiti, F., 2014. Calibration of an acoustic pipe sensor through bedload traps in a glacierized basin. CATENA 121, 222–231. https://doi.org/10.1016/j.catena.2014.05.021

Dietze, M., Lagarde, S., Halfi, E., Laronne, J.B., Turowski, J.M., 2019. Joint Sensing of Bedload Flux and Water Depth by Seismic Data Inversion. Water Resources Research 55, 9892–9904. https://doi.org/10.1029/2019WR026072

Downing, J., 2010. Acoustic gravel-momentum sensor. US Geological Survey Scientific Investigations Report 5091, 143–158.

Elgueta-Astaburuaga, M.A., Hassan, M.A., 2019. Sediment storage, partial transport, and the evolution of an experimental gravel bed under changing sediment supply regimes. Geomorphology 330, 1–12. https://doi.org/10.1016/j.geomorph.2018.12.018

Elgueta-Astaburuaga, M.A., Hassan, M.A., Saletti, M., Clarke, G.K.C., 2018. The Effect of Episodic Sediment Supply on Bedload Variability and Sediment Mobility. Water Resources Research 54, 6319–6335. https://doi.org/10.1029/2017WR022280

FOEN, 2010. Hydrologisches Jahrbuch Schweiz. Federal Office for the Environment (FOEN).

FOEN, (ed.), 2021. Effects of climate change on Swiss water bodies. Hydrology, water ecology and water management. (Environmental studies No. 2101:125p.). Federal Office for the Environment FOEN, Bern.

Freudiger, D., Frielingsdorf, B., Stahl, K., Steinbrich, A., Weiler, M., Griessinger, N., Seibert, J., 2016. Das Potential meteorologischer Rasterdatensätze für die Modellierung der Schneedecke alpiner Einzugsgebiete. Hydrologie und Wasserbewirtschaftung 60, 353–367. https://doi.org/10.5675/HyWa_2016,6_1

Gabbud, C., Bakker, M., Clémençon, M., Lane, S.N., 2019. Hydropower Flushing Events Cause Severe Loss of Macrozoobenthos in Alpine Streams. Water Resources Research 55, 10056–10081. https://doi.org/10.1029/2019WR024758

Geay, T., Belleudy, P., Gervaise, C., Habersack, H., Aigner, J., Kreisler, A., Seitz, H., Laronne, J.B., 2017. Passive acoustic monitoring of bed load discharge in a large gravel bed river. Journal of Geophysical Research: Earth Surface 122, 528–545. https://doi.org/10.1002/2016JF004112

Gomez, B., 1991. Bedload transport. Earth-Science Reviews 31, 89–132.

Gomez, B., Church, M., 1989. An assessment of bed load sediment transport formulae for gravel bed rivers. Water Resources Research 25, 1161–1186.

Gomez, B., Naff, R.L., Hubbell, D.W., 1989. Temporal variations in bedload transport rates associated with the migration of bedforms. Earth Surface Processes and Landforms 14, 135–156.

Gray, J.R., Laronne, J.B., Marr, J.D., 2010. Bedload-surrogate monitoring technologies. US Department of the Interior, US Geological Survey.

Gribovszki, Z., Szilágyi, J., Kalicz, P., 2010. Diurnal fluctuations in shallow groundwater levels and streamflow rates and their interpretation – A review. Journal of Hydrology 385, 371–383. https://doi.org/10.1016/j.jhydrol.2010.02.001

Habersack, H., Kreisler, A., Rindler, R., Aigner, J., Seitz, H., Liedermann, M., Laronne, J.B., 2017. Integrated automatic and continuous bedload monitoring in gravel bed rivers. Geomorphology, SEDIMENT DYNAMICS IN ALPINE BASINS 291, 80–93. https://doi.org/10.1016/j.geomorph.2016.10.020

Hauer, C., Wagner, B., Aigner, J., Holzapfel, P., Flödl, P., Liedermann, M., Tritthart, M., Sindelar, C., Pulg, U., Klösch, M., Haimann, M., Donnum, B.O., Stickler, M., Habersack, H., 2018. State of the art, shortcomings and future challenges for a sustainable sediment management in hydropower: A review. Renewable and Sustainable Energy Reviews 98, 40–55. https://doi.org/10.1016/j.rser.2018.08.031

Helley, E.J., Smith, W., 1971. Development and calibration of a pressure-difference bedload sampler.

Heritage, G., Entwistle, N.S., Milan, D., 2019. Evidence of non-contiguous flood driven coarse sediment transfer and implications for sediment management, in: E-Proceedings of the 38th IAHR World Congress. International Association for Hydro-Environment Engineering and Research.

Hinderer, M., Kastowski, M., Kamelger, A., Bartolini, C., Schlunegger, F., 2013. River loads and modern denudation of the Alps — A review. Earth-Science Reviews 118, 11–44. https://doi.org/10.1016/j.earscirev.2013.01.001

Hirschberg, J., Fatichi, S., Bennett, G.L., McArdell, B.W., Peleg, N., Lane, S.N., Schlunegger, F., Molnar, P., 2021. Climate Change Impacts on Sediment Yield and Debris-Flow Activity in an Alpine Catchment. Journal of Geophysical Research: Earth Surface 126, e2020JF005739. https://doi.org/10.1029/2020JF005739

Hoey, T.B., Sutherland, A.J., 1991. Channel morphology and bedload pulses in braided rivers: a laboratory study. Earth Surface Processes and Landforms 16, 447–462.

Horton, P., Schaefli, B., Mezghani, A., Hingray, B., Musy, A., 2006. Assessment of climate-change impacts on alpine discharge regimes with climate model uncertainty. Hydrological Processes 20, 2091–2109. https://doi.org/10.1002/hyp.6197

Huggel, C., Clague, J.J., Korup, O., 2012. Is climate change responsible for changing landslide activity in high mountains? Earth Surface Processes and Landforms 37, 77–91. https://doi.org/10.1002/esp.2223

James, M.R., Antoniazza, G., Robson, S., Lane, S.N., 2020. Mitigating systematic error in topographic models for geomorphic change detection: accuracy, precision and

considerations beyond off-nadir imagery. Earth Surface Processes and Landforms 45, 2251–2271. https://doi.org/10.1002/esp.4878

Kammerlander, J., Gems, B., Kößler, D., Aufleger, M., 2017. Effect of bed load supply on sediment transport in mountain streams. International Journal of Sediment Research 32, 240–252. https://doi.org/10.1016/j.ijsrc.2017.03.004

Kreisler, A., Moser, M., Aigner, J., Rindler, R., Tritthart, M., Habersack, H., 2017. Analysis and classification of bedload transport events with variable process characteristics. Geomorphology, SEDIMENT DYNAMICS IN ALPINE BASINS 291, 57–68. https://doi.org/10.1016/j.geomorph.2016.06.033

Lane, S.N., Bakker, M., Gabbud, C., Micheletti, N., Saugy, J.-N., 2017. Sediment export, transient landscape response and catchment-scale connectivity following rapid climate warming and Alpine glacier recession. Geomorphology 277, 210–227.

Lane, S.N., Borgeaud, L., Vittoz, P., 2016. Emergent geomorphic–vegetation interactions on a subalpine alluvial fan. Earth Surface Processes and Landforms 41, 72–86. https://doi.org/10.1002/esp.3833

Lane, S.N., Gentile, A., Goldenschue, L., 2020. Combining UAV-Based SfM-MVS Photogrammetry with Conventional Monitoring to Set Environmental Flows: Modifying Dam Flushing Flows to Improve Alpine Stream Habitat. Remote Sensing 12, 3868. https://doi.org/10.3390/rs12233868

Lane, S.N., Nienow, P.W., 2019. Decadal-Scale Climate Forcing of Alpine Glacial Hydrological Systems. Water Resources Research 55, 2478–2492. https://doi.org/10.1029/2018WR024206

Lauffer, H., Sommer, N., 1982. Studies on sediment transport in mountain streams of the Eastern Alps, in: Proc., International Commission on Large Dams, 14th Congress, Rio de Janiero. International Association for Hydraulic Research, Rio de Janeiro, Brazil. pp. 431–453.

Lenzi, M.A., D'Agostino, V., Billi, P., 1999. Bedload transport in the instrumented catchment of the Rio Cordon: Part I: Analysis of bedload records, conditions and threshold of bedload entrainment. Catena 36, 171–190.

Li, D., Lettenmaier, D.P., Margulis, S.A., Andreadis, K., 2019. The Role of Rain-on-Snow in Flooding Over the Conterminous United States. Water Resources Research 55, 8492–8513. https://doi.org/10.1029/2019WR024950

Mächler, E., Salyani, A., Walser, J.-C., Larsen, A., Schaefli, B., Altermatt, F., Ceperley, N., 2021. Environmental DNA simultaneously informs hydrological and biodiversity characterization of an Alpine catchment. Hydrology and Earth System Sciences 25, 735–753. https://doi.org/10.5194/hess-25-735-2021

Mancini, D., Lane, S.N., 2020. Changes in sediment connectivity following glacial debuttressing in an Alpine valley system. Geomorphology 352, 106987. https://doi.org/10.1016/j.geomorph.2019.106987

Mao, L., 2018. The effects of flood history on sediment transport in gravel-bed rivers. Geomorphology 322, 196–205. https://doi.org/10.1016/j.geomorph.2018.08.046

Mao, L., 2012. The effect of hydrographs on bed load transport and bed sediment spatial arrangement. Journal of Geophysical Research: Earth Surface 117. https://doi.org/10.1029/2012JF002428

Mao, L., Carrillo, R., Escauriaza, C., Iroume, A., 2016. Flume and field-based calibration of surrogate sensors for monitoring bedload transport. Geomorphology 253, 10–21. https://doi.org/10.1016/j.geomorph.2015.10.002

Mao, L., Dell'Agnese, A., Huincache, C., Penna, D., Engel, M., Niedrist, G., Comiti, F., 2014. Bedload hysteresis in a glacier- fed mountain river. Earth Surface Processes and Landforms 39, 964–976. https://doi.org/10.1002/esp.3563

Masteller, C.C., Finnegan, N.J., Turowski, J.M., Yager, E.M., Rickenmann, D., 2019. History-Dependent Threshold for Motion Revealed by Continuous Bedload Transport Measurements in a Steep Mountain Stream. Geophysical Research Letters 46, 2583–2591. https://doi.org/10.1029/2018GL081325

Messenzehl, K., Viles, H., Otto, J.-C., Ewald, A., Dikau, R., 2018. Linking rock weathering, rockwall instability and rockfall supply on talus slopes in glaciated hanging valleys (Swiss Alps). Permafrost and Periglacial Processes 29, 135–151. https://doi.org/10.1002/ppp.1976

MeteoSwiss, 2019. Daily Precipitation (final analysis): Rhires D. Documentation of MeteoSwiss, Grid-Data Products.

MeteoSwiss, 2017. Daily Mean, Minimum and Maximum Temperature: TabsD, TminD, TmaxD. Documentation of MeteoSwiss Grid-Data Products.

Micheletti, N., Lambiel, C., Lane, S.N., 2015. Investigating decadal- scale geomorphic dynamics in an alpine mountain setting. Journal of Geophysical Research: Earth Surface 120, 2155–2175.

Micheletti, N., Lane, S.N., 2016. Water yield and sediment export in small, partially glaciated Alpine watersheds in a warming climate. Water Resources Research 52, 4924–4943.

Michelon, A., Benoit, L., Beria, H., Ceperley, N., Schaefli, B., 2021. Benefits from high-density rain gauge observations for hydrological response analysis in a small alpine catchment. Hydrology and Earth System Sciences 25, 2301–2325. https://doi.org/10.5194/hess-25-2301-2021

Mikovski, M., 2021. polfitzero [Matlab function]. https://fr.mathworks.com/matlabcentral/fileexchange/35401-polyfitzero.

Misset, C., Recking, A., Legout, C., Bakker, M., Gimbert, F., Geay, T., Zanker, S., 2021. Using Continuous Turbidity and Seismic Measurements to Unravel Sediment Provenance and Interaction Between Suspended and Bedload Transport in an Alpine Catchment. Geophysical Research Letters 48, e2020GL090696. https://doi.org/10.1029/2020GL090696

Mizuyama, T., Laronne, J.B., Nonaka, M., Sawada, T., Satofuka, Y., Matsuoka, M., Yamashita, S., Sako, Y., Tamaki, S., Watari, M., 2010. Calibration of a passive acoustic bedload monitoring system in Japanese mountain rivers. US Geological Survey Scientific Investigations Report 5091, 296–318.

Musselman, K.N., Clark, M.P., Liu, C., Ikeda, K., Rasmussen, R., 2017. Slower snowmelt in a warmer world. Nature Clim Change 7, 214–219. https://doi.org/10.1038/nclimate3225

Musselman, K.N., Lehner, F., Ikeda, K., Clark, M.P., Prein, A.F., Liu, C., Barlage, M., Rasmussen, R., 2018. Projected increases and shifts in rain-on-snow flood risk over western North America. Nature Climate Change 8, 808–812. https://doi.org/10.1038/s41558-018-0236-4

Mutzner, R., Weijs, S.V., Tarolli, P., Calaf, M., Oldroyd, H.J., Parlange, M.B., 2015. Controls on the diurnal streamflow cycles in two subbasins of an alpine headwater catchment. Water Resources Research 51, 3403–3418. https://doi.org/10.1002/2014WR016581

Nicollier, T., Rickenmann, D., Boss, S., Travaglini, E., Hartlieb, A., 2020. Calibration of the Swiss plate geophone system at the Zinal field site with direct bedload samples and results from controlled flume experiments. Presented at the SEDHYD River Flow 2020 Conference., p. 8.

Nicollier, T., Rickenmann, D., Hartlieb, A., 2021. Field and flume measurements with the impact plate: effect of bedload grain-size distribution on signal response. Earth Surface Processes and Landforms n/a. https://doi.org/10.1002/esp.5117

Nicollier, T., Rickenmann, D., Hartlieb, A., 2019. Calibration of the Swiss plate geophone system at the Albula field site with direct bedload samples and comparison with controlled flume experiments, in: SEDHYD 2019 Conference, Federal Interagency Sedimentation and Hydrologic, Modeling Conference. p. Paper 345, 8 p.

Parker, G., Dhamotharan, S., Stefan, H., 1982. Model experiments on mobile, paved gravel bed streams. Water Resources Research 18, 1395–1408.

Perolo, P., Bakker, M., Gabbud, C., Moradi, G., Rennie, C., Lane, S.N., 2019. Subglacial sediment production and snout marginal ice uplift during the late ablation season of a temperate valley glacier. Earth Surface Processes and Landforms.

Piton, G., Recking, A., 2017. The concept of travelling bedload and its consequences for bedload computation in mountain streams. Earth Surface Processes and Landforms 42, 1505–1519. https://doi.org/10.1002/esp.4105

Porter, P.R., Smart, M.J., Irvine-Fynn, T.D.L., 2019. Glacial Sediment Stores and Their Reworking, in: Heckmann, T., Morche, D. (Eds.), Geomorphology of Proglacial Systems: Landform and Sediment Dynamics in Recently Deglaciated Alpine Landscapes, Geography of the Physical Environment. Springer International Publishing, Cham, pp. 157–176. https://doi.org/10.1007/978-3-319-94184-4_10

Pralong, M.R., Turowski, J.M., Rickenmann, D., Zappa, M., 2015. Climate change impacts on bedload transport in alpine drainage basins with hydropower exploitation. Earth Surface Processes and Landforms 40, 1587–1599. https://doi.org/10.1002/esp.3737

Rainato, R., Mao, L., García-Rama, A., Picco, L., Cesca, M., Vianello, A., Preciso, E., Scussel, G.R., Lenzi, M.A., 2017. Three decades of monitoring in the Rio Cordon instrumented basin: Sediment budget and temporal trend of sediment yield. Geomorphology, SEDIMENT DYNAMICS IN ALPINE BASINS 291, 45–56. https://doi.org/10.1016/j.geomorph.2016.03.012

Ravanel, L., Deline, P., 2011. Climate influence on rockfalls in high-Alpine steep rockwalls: The north side of the Aiguilles de Chamonix (Mont Blanc massif) since the end of the 'Little Ice Age.' The Holocene 21, 357–365.

Recking, A., 2013. An analysis of nonlinearity effects on bed load transport prediction. Journal of Geophysical Research: Earth Surface 118, 1264–1281. https://doi.org/10.1002/jgrf.20090

Reid, D.A., Hassan, M.A., Bird, S., Hogan, D., 2019. Spatial and temporal patterns of sediment storage over 45 years in Carnation Creek, BC, a previously glaciated mountain catchment. Earth Surface Processes and Landforms 44, 1584–1601. https://doi.org/10.1002/esp.4595

Rickenmann, D., 2020. Effect of Sediment Supply on Cyclic Fluctuations of the Disequilibrium Ratio and Threshold Transport Discharge, Inferred From Bedload Transport Measurements Over 27 Years at the Swiss Erlenbach Stream. Water Resources Research 56, e2020WR027741. https://doi.org/10.1029/2020WR027741

Rickenmann, D., 2018. Variability of Bed Load Transport During Six Summers of Continuous Measurements in Two Austrian Mountain Streams (Fischbach and Ruetz). Water Resources Research 54, 107–131. https://doi.org/10.1002/2017WR021376

Rickenmann, D., 2017. Bedload transport measurements with geophones, hydrophones and underwater microphones (passive acoustic methods). Gravel Bed Rivers and Disasters, Wiley & Sons, Chichester, UK 185–208.

Rickenmann, D., 2012. Alluvial Steep Channels: Flow Resistance, Bedload Transport Prediction, and Transition to Debris Flows, in: Gravel-Bed Rivers. John Wiley & Sons, Ltd, pp. 386–397. https://doi.org/10.1002/9781119952497.ch28

Rickenmann, D., 1997. Sediment transport in Swiss torrents. Earth Surface Processes and Landforms 22, 937–951. https://doi.org/10.1002/(SICI)1096-9837(199710)22:10<937::AID-ESP786>3.0.CO;2-R

Rickenmann, D., Antoniazza, G., Wyss, C.R., Fritschi, B., Boss, S., 2017. Bedload transport monitoring with acoustic sensors in the Swiss Albula mountain river. Proceedings of the International Association of Hydrological Sciences 375, 5.

Rickenmann, D., Fritschi, B., 2017. Bedload transport measurements with impact plate geophones in two Austrian mountain streams (Fischbach and Ruetz): system calibration, grain size estimation, and environmental signal pick-up. Earth Surface Dynamics 5.

Rickenmann, D., Koschni, A., 2010. Sediment loads due to fluvial transport and debris flows during the 2005 flood events in Switzerland. Hydrological Processes: An International Journal 24, 993–1007.

Rickenmann, D., McArdell, B.W., 2008. Calibration of piezoelectric bedload impact sensors in the Pitzbach mountain stream. Geodinamica Acta 21, 35–52.

Rickenmann, D., McArdell, B.W., 2007. Continuous measurement of sediment transport in the Erlenbach stream using piezoelectric bedload impact sensors. Earth Surface Processes and Landforms 32, 1362–1378. https://doi.org/10.1002/esp.1478

Rickenmann, D., Nicollier, T., Boss, S., Badoux, A., 2020. Four years of bedload transport measurements in the Swiss Mountain River Albula. River flow 2020. Proceedings of the 10th conference on fluvial hydraulics 1749–1755. https://doi.org/10.1201/b22619-245

Rickenmann, D., Recking, A., 2011. Evaluation of flow resistance in gravel- bed rivers through a large field data set. Water Resources Research 47.

Rickenmann, D., Turowski, J.M., Fritschi, B., Klaiber, A., Ludwig, A., 2012. Bedload transport measurements at the Erlenbach stream with geophones and automated basket samplers. Earth Surface Processes and Landforms 37, 1000–1011.

Rickenmann, D., Turowski, J.M., Fritschi, B., Wyss, C., Laronne, J., Barzilai, R., Reid, I., Kreisler, A., Aigner, J., Seitz, H., 2014. Bedload transport measurements with impact plate geophones: comparison of sensor calibration in different gravel- bed streams. Earth Surface Processes and Landforms 39, 928–942.

Rigby, J.R., Wren, D.G., Kuhnle, R.A., 2016. Passive Acoustic Monitoring of Bed Load for Fluvial Applications. Journal of Hydraulic Engineering 142, 02516003. https://doi.org/10.1061/(ASCE)HY.1943-7900.0001122

Roth, D.L., Brodsky, E.E., Finnegan, N.J., Rickenmann, D., Turowski, J.M., Badoux, A., 2016. Bed load sediment transport inferred from seismic signals near a river. Journal of Geophysical Research: Earth Surface 121, 725–747. https://doi.org/10.1002/2015JF003782

Schneider, J.M., Rickenmann, D., Turowski, J.M., Bunte, K., Kirchner, J.W., 2015. Applicability of bed load transport models for mixed-size sediments in steep streams considering macro-roughness. Water Resources Research 51, 5260–5283. https://doi.org/10.1002/2014WR016417

Sims, A.J., Rutherfurd, I.D., 2017. Management responses to pulses of bedload sediment in rivers. Geomorphology, Anthropogenic Sedimentation 294, 70–86. https://doi.org/10.1016/j.geomorph.2017.04.010

Singh, A., Fienberg, K., Jerolmack, D.J., Marr, J., Foufoula- Georgiou, E., 2009. Experimental evidence for statistical scaling and intermittency in sediment transport rates. Journal of Geophysical Research: Earth Surface 114.

Speerli, J., Bachmann, A., Bieler, S., Schumacher, A., Gysin, S., 2020. Auswirkungen des Klimawanderls auf den Sedimenttransport. Hochschule für Technik, Rapperswil.

Spreafico, M., Lehmann, C., 1994. Sediment transport observations in Switzerland. IAHS Publications-Series of Proceedings and Reports-Intern Assoc Hydrological Sciences 224, 259–268.

Stoffel, M., Mendlik, T., Schneuwly-Bollschweiler, M., Gobiet, A., 2014. Possible impacts of climate change on debris-flow activity in the Swiss Alps. Climatic Change 122, 141–155.

Thornton, J.M., Brauchli, T., Mariethoz, G., Brunner, P., 2021. Efficient multi-objective calibration and uncertainty analysis of distributed snow simulations in rugged alpine terrain. Journal of Hydrology 598, 126241. https://doi.org/10.1016/j.jhydrol.2021.126241

Tockner, K., Malard, F., Uehlinger, U., Ward, J.V., 2002. Nutrients and organic matter in a glacial river—floodplain system (Val Roseg, Switzerland). Limnology and Oceanography 47, 266–277. https://doi.org/10.4319/lo.2002.47.1.0266

Turowski, J.M., Rickenmann, D., Dadson, S.J., 2010. The partitioning of the total sediment load of a river into suspended load and bedload: a review of empirical data. Sedimentology 57, 1126–1146. https://doi.org/10.1111/j.1365-3091.2009.01140.x

Venditti, J.G., Dietrich, W.E., Nelson, P.A., Wydzga, M.A., Fadde, J., Sklar, L., 2010. Mobilization of coarse surface layers in gravel- bedded rivers by finer gravel bed load. Water Resources Research 46.

Wang, Z.-Y., Lee, J.H., Melching, C.S., 2014. River dynamics and integrated river management. Springer Science & Business Media.

Wilcock, P.R., Crowe, J.C., 2003. Surface-based transport model for mixed-size sediment. Journal of Hydraulic Engineering 129, 120–128.

Wyss, C.R., Rickenmann, D., Fritschi, B., Turowski, J.M., Weitbrecht, V., Boes, R.M., 2016a. Laboratory flume experiments with the Swiss plate geophone bed load monitoring system: 1. Impulse counts and particle size identification. Water Resources Research 52, 7744–7759. https://doi.org/10.1002/2015WR018555

Wyss, C.R., Rickenmann, D., Fritschi, B., Turowski, J.M., Weitbrecht, V., Travaglini, E., Bardou, E., Boes, R.M., 2016b. Laboratory flume experiments with the Swiss plate geophone bed load monitoring system: 2. Application to field sites with direct bed load samples. Water Resources Research 52, 7760–7778. https://doi.org/10.1002/2016WR019283

Wyss, C.R., Rickenmann Dieter, Fritschi Bruno, Turowski Jens M., Weitbrecht Volker, Boes Robert M., 2016c. Measuring Bed Load Transport Rates by Grain-Size Fraction Using the Swiss Plate Geophone Signal at the Erlenbach. Journal of Hydraulic Engineering 142, 04016003. https://doi.org/10.1061/(ASCE)HY.1943-7900.0001090

Yager, E.M., Kenworthy, M., Monsalve, A., 2015. Taking the river inside: Fundamental advances from laboratory experiments in measuring and understanding bedload transport processes. Geomorphology, Laboratory Experiments in Geomorphology 46th Annual Binghamton Geomorphology Symposium 18-20 September 2015 244, 21–32. https://doi.org/10.1016/j.geomorph.2015.04.002